AFRL-IF-RS-TR-2003-80
Final Technical Report
April 2003

MICROMACHINED RADIO FREQUENCY (RF) SWITCHES AND TUNABLE CAPACITORS FOR HIGHER PERFORMANCE SECURE COMMUNICATIONS SYSTEMS

Rockwell Scientific Company

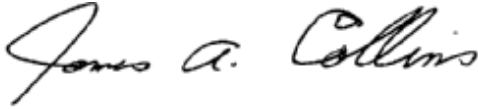*APPROVED FOR PUBLIC RELEASE; DISTRIBUTION UNLIMITED.*

The views and conclusions contained in this document are those of the authors and should not be interpreted as necessarily representing the official policies, either expressed or implied, of the Defense Advanced Research Projects Agency or the U.S. Government.

AIR FORCE RESEARCH LABORATORY
INFORMATION DIRECTORATE
ROME RESEARCH SITE
ROME, NEW YORK

This report has been reviewed by the Air Force Research Laboratory, Information Directorate, Public Affairs Office (IFOIPA) and is releasable to the National Technical Information Service (NTIS). At NTIS it will be releasable to the general public, including foreign nations.

AFRL-IF-RS-TR-2003-80 has been reviewed and is approved for publication.

APPROVED:

DAVID C. WILLIAMSON
Project Engineer

FOR THE DIRECTOR:

JAMES A. COLLINS, Acting Chief
Information Technology Division
Information Directorate

REPORT DOCUMENTATION PAGE		*Form Approved* *OMB No. 074-0188*
Public reporting burden for this collection of information is estimated to average 1 hour per response, including the time for reviewing instructions, searching existing data sources, gathering and maintaining the data needed, and completing and reviewing this collection of information. Send comments regarding this burden estimate or any other aspect of this collection of information, including suggestions for reducing this burden to Washington Headquarters Services, Directorate for Information Operations and Reports, 1215 Jefferson Davis Highway, Suite 1204, Arlington, VA 22202-4302, and to the Office of Management and Budget, Paperwork Reduction Project (0704-0188), Washington, DC 20503		

1. AGENCY USE ONLY (Leave blank)	2. REPORT DATE APRIL 2003	3. REPORT TYPE AND DATES COVERED Final Sep 97 - Aug 02

4. TITLE AND SUBTITLE MICROMACHINED RADIO FREQUENCY (RF) SWITCHES AND TUNABLE CAPACITORS FOR HIGHER PERFORMANCE SECURE COMMUNICATIONS SYSTEMS	5. FUNDING NUMBERS C - F30602-97-C-0091 PE - 63739E PR - E117 TA - 00 WU - 14
6. AUTHOR(S) Jeff F. DeNatale	

7. PERFORMING ORGANIZATION NAME(S) AND ADDRESS(ES) Rockwell Scientific Company 1049 Camino Dos Rios Thousand Oaks California 91360	8. PERFORMING ORGANIZATION REPORT NUMBER

9. SPONSORING / MONITORING AGENCY NAME(S) AND ADDRESS(ES) Defense Advanced Research Projects Agency AFRL/IFTC 3701 North Fairfax Drive 26 Electronic Parkway Arlington Virginia 22203-1714 Rome New York 13441-4514	10. SPONSORING / MONITORING AGENCY REPORT NUMBER AFRL-IF-RS-TR-2003-80

11. SUPPLEMENTARY NOTES

AFRL Project Engineer: David C. Williamson/IFTC/(315) 330-7324/ David.Williamson@rl.af.mil

12a. DISTRIBUTION / AVAILABILITY STATEMENT APPROVED FOR PUBLIC RELEASE; DISTRIBUTION UNLIMITED.	12b. DISTRIBUTION CODE

13. ABSTRACT *(Maximum 200 Words)*
The purpose of this program is to develop and demonstrate MEMS for RF communications applications. The development activities focus on two MEMS devices: RF Switches and Tunable Capacitors. The application of these components to RF subsystems offers the potential for substantial improvements in a number of performance metrics, including size, weight, power consumption, and parts count. The advantages of MEMS technology will be demonstrated in this program by insertions of these devices into three military communication subsystems, corresponding to the three following technical tasks: 1) MEM Tunable Capacitor-based UHF Tracking Filter for the F-22 Antenna Interface Unit (AIU), 2) MEM RF Switch-based VHF Tracking Filter for the Comanche Helicopter AIU, and 3) MEM Tunable RF Filter (incorporating both MEM RF Switches and Tunable Capacitors) for the Receiver Pre-selector in the Joint Services ARC-210 Radio. Demonstration of MEMS RF switches in the space environment and the reliability assessment of RF Switches and Capacitors are also included.

14. SUBJECT TERMS Microelectromechanical Systems, MEMS, Switches, Tunable Capacitors, Communications, MEMS Reliability, Filters	15. NUMBER OF PAGES 66
	16. PRICE CODE

17. SECURITY CLASSIFICATION OF REPORT UNCLASSIFIED	18. SECURITY CLASSIFICATION OF THIS PAGE UNCLASSIFIED	19. SECURITY CLASSIFICATION OF ABSTRACT UNCLASSIFIED	20. LIMITATION OF ABSTRACT UL

NSN 7540-01-280-5500

Standard Form 298 (Rev. 2-89)
Prescribed by ANSI Std. Z39-18
298-102

Table of Contents

List of Figures

List of Tables

1 Executive Summary

This report describes the progress in a multi-year program to demonstrate the utility of RF MEMS devices in military communications subsystems. This has illustrated the advantageous performance characteristics of the MEMS devices and demonstrated their resulting subsystem-level benefits. The work also highlighted the technical areas of the MEMS devices that will require additional maturation before insertion into fielded DoD systems.

The program focused on two device types: a metal-contact MEMS RF switch and a Si-based MEMS voltage tunable capacitor. Considerable effort went into the development of the component devices to achieve the combined flowdown requirements from the demonstration subsystems. For the MEMS RF switch, devices were successfully implemented with low insertion loss, high linearity, low power consumption, and rapid switching times. Packaging methodology was found to significantly impact device performance, and a packaging process was developed that preserved high-quality device operation. For the tunable capacitor, a Si-based lateral motion intedigitated comb device was adopted to provide wide tuning range and sufficient base capacitance. While the original goals anticipated only a 4x capacitance tuning requirement, it was found that a significantly higher level was required to accommodate package parasitics. Ultimate devices achieved tuning ratios in excess of 8x, base capacitance values of approximately 2pF, and series resistance below 1 Ohm. The packaging of the tunable capacitors was found to be significantly less demanding than the RF switch owing to its lack of contacting surfaces during operation.

The device insertions were conducted for two specific military communications subsystems. For the MEMS RF switch, a VHF 2-pole filter was implemented based on the requirements of the RA-66 Comanche Antenna Interface Unit (AIU). This adapted switched capacitor bank architecture replaced the PIN diodes in the existing circuit with MEMS RF switches. Demonstration filters were fabricated and tested. These achieved significant improvements in filter linearity and quiescent power consumption relative to the present PIN diode based circuit. The MEMS-based filter met all RF requirements for the 2-pole filter circuit.

The insertion vehicle for the tunable capacitor device was a 2-pole UHF filter assembly targeting the operational requirements for the F-22 AIU. This used the MEMS tunable capacitors in place of arrays of semiconductor varactor diodes used in the present circuit. The MEMS-based demonstration circuits were implemented, and showed near full-octave tuning with just two MEMS devices. This represented an 86% parts count reduction relative to the varactor-based circuit. The MEMS-based circuit was slightly out of spec at the extremes of the tuning range due to higher series resistance than desired. Temporal response was significantly longer than for the varactor-based circuit, and was dominated by mechanical ringing of the MEMS device. Modifications to the device have been identified that can improve on this metric.

As part of the program, support was provided for the Picosat miniature satellite demonstrations. These experiments addressed validation of the concept of miniature networked satellites. Low-power communications boards and MEMS switches were provided by RSC to support these missions. These resulted in successful demonstrations of both the communications aspects of the concept, as well as validating the operation of MEMS switches in a space environment.

2   Background and Program Goals

High-performance military RF communications systems can require complex electronics to achieve the necessary tuning and filtering functions. These requirements can become even more severe in environments with multiple transmit and receive systems collocated on a single platform ("cosite"). At present, these functions are typically achieved using solid-state devices, such as PIN Diodes, GaAs FET's and varactor diodes. Limitations of these components, however, can impose significant performance impacts on the system in terms of RF characteristics (insertion loss, return loss, linearity), cost, complexity, and power consumption.

Microelectromechanical systems (MEMS) represents an emerging technology that offers attractive performance capabilities in a broad range of applications. In contrast to semiconductor electronics that use transport of charge carriers to achieve their functionality, MEMS devices use the physical motion of mechanical elements at micron-scale dimensions to achieve this end. For many applications, this use of mechanical operation can provide efficient and elegant solutions, especially to sensing and actuation functions that require direct interface with the physical environment.

One area of particular interest for MEMS technology is in RF devices. Here, small physical displacements can be used to generate large excursions in RF response. Extensive work in RF switches, tunable capacitors, micromechanical resonators, and micromachined inductors have clearly demonstrated the potential of RF MEMS devices. In particular, MEMS switches and tunable capacitors have been identified as devices that could provide significant performance enhancements to military communications and radar applications.

While a number of device-level RF MEMS development activities have been conducted, there has been very little work to date in assessing the issues and impacts of these devices in actual DoD systems and subsystems. A number of key issues become important in such insertions to evaluate and validate the benefits of RF MEMS, encompassing device, package, and interface considerations. This program was aimed at characterizing these issues and demonstrating the utility of RF MEMS devices in DoD subsystem insertions. The thrusts of the effort addressed both the RF MEMS devices as well as their insertion into prototype military communications subsystems. These efforts focused on two specific MEMS devices: RF switches and tunable capacitors. The application of these components to RF subsystems offers the potential for substantial improvements in a number of performance metrics, including size, weight, power consumption, and parts count. The advantages of MEMS technology were benchmarked relative to conventional semiconductor electronics by insertion of these devices into two specific military communication subsystems:

- MEM Tunable Capacitor-based UHF Tracking Filter for the F22 Antenna Interface Unit (AIU)
- MEM RF Switch-based VHF Tracking Filter for the Comanche Helicopter AIU.

A third demonstration was originally planned that would incorporate both the MEMS RF switch and tunable capacitor devices into a single communications circuit. The vehicle for this was to be the Tunable RF Filter for the Receiver Pre-selector in the Joint Services ARC-210 Radio. During the course of the program, a significant amount of additional development was required on the component devices beyond the original plan, which precluded execution of the ARC-210 demonstration. From the measured characteristics of the switch and tunable capacitor devices generated from the other two demonstrations, however, an accurate assessment of the combined device architecture in the ARC-210 circuit could be generated.

The program was conducted as a joint effort between Rockwell Scientific Company (RSC, formerly Rockwell Science Center) in Thousand Oaks, CA, and Rockwell Collins Inc. (RCI), in Cedar Rapids, IA. RSC was the prime contractor on the program, and took lead on the MEMS device development activities. RCI lead the design and integration and test of the demonstration filter assemblies.

3   MEMS RF Switch Device Development

The MEMS switch technology utilized in this program's switched-filter demonstration was based on a metal-contact microrelay previously developed by RSC.   Under this program, the switch and packaging technologies were optimized to provide the RF performance required under the filter subcircuit demonstration. The nominal packaged device specifications, derived through flowdown of the circuit requirements from the Comanche VHF filter, established the target goals for the RF switch device. These specifications are:

- Max. series resistance, Rs, (on): 1.8 Ohm (0.5 GHz)
- Max. series capacitance, Cs, (off): 0.5 pF (0.5 GHz)
- Min. 3rd Order Intercept, IP3: 50 dBm
- Effective RF current and voltage, $I_{RF,}$ V_{RF} (survive): 0.2 A, 10.4 V rms
- Effective RF current and voltage, $I_{RF,}$ V_{RF} (operation): 0.03 A, 2.1 V rms
- Max. switching Time: 15 usec

3.1   RSC MEM Switch Design and Fabrication

The structure and operation of the RSC microrelay are shown in Figure 3.1.   This microrelay is a surface-micromachined structure fabricated from thin films deposited atop the substrate. The relay consists of a metal bridge bar that is suspended over a broken RF signal line on the substrate. This bridge bar is suspended via insulating beams that attach to a mechanical structure consisting of two plates and two pairs of folded-beam springs, both also made of insulators. This entire suspended structure is anchored to the substrate via four legs at the ends of the springs. The device covers an area of size ~250 μm x 250 μm, with the suspended structure sitting a few microns above the substrate plane. The microrelay allows RF signal line widths of 20-40 μm.
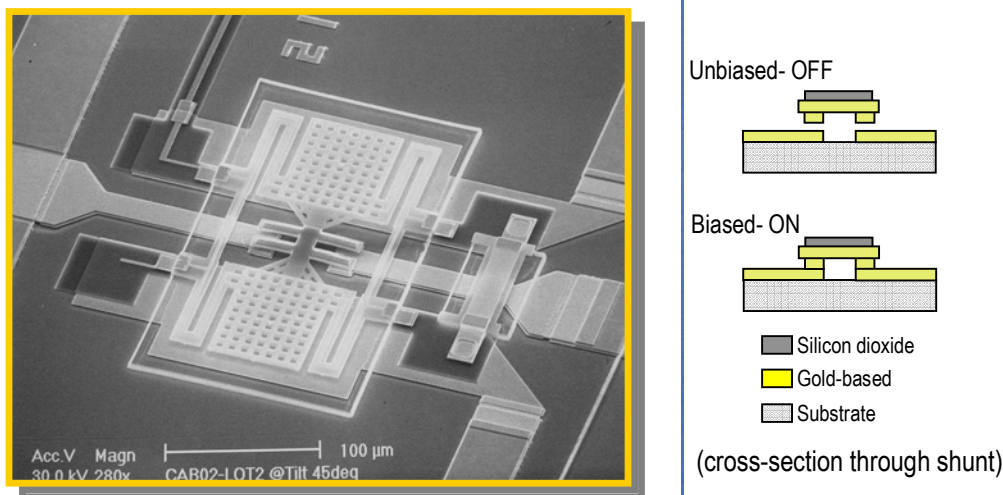
Fig. 3.1: RSC MEMS switch and schematic of switch geometry in Unbiased (OFF) and Biased (ON) states.

Relay functionality is controlled by the application of a bias voltage, which electrostatically actuates the bridge-supporting mechanical structure. In its unbiased state, the structure is suspended so the bridge bar is separated from signal line via an airgap and the relay is non-conducting (OFF). The effective capacitance for this switch state, set by coupling across a micron-sized airgap, is ~1.75 fF. When a threshold bias is applied, the structure is pulled down so the bridge bar contacts the signal line and the relay is conducting (ON). The effective resistance for this state, formed by contacting metal surfaces, is ~1 Ω. The relay is switched ON to OFF by reducing the control voltage to allow the elastically deflected springs of the mechanical structure to pull the structure and bridge bar upward.

The RSC relay is fabricated by surface micromachining techniques, using low-temperature (< 250°C) thin films deposited atop the substrate. Details of the fabrication process are summarized schematically in Fig 3.2. First, signal lines found on the substrate are defined by lift-off patterning of evaporated Au films. A sacrificial layer is then formed from a spun and planarized organic layer. This organic layer serves as a platform for building the relay mechanical structure. Windows etched in the organic define the anchor regions for the mechanical structure. The electrical bridging bar is then defined atop the organic by lift-off patterning of evaporated gold. Next, the mechanical structure is constructed from plasma enhanced chemical vapor deposition (PECVD) of the dielectric structural layer, lift-off of the drive metal patterns, and etching of the PECVD film. The entire relay microstructure is made freestanding in the final fabrication step by isotropic etching of the sacrificial organic.

This fabrication technology offers versatility in substrate selection. Switch devices can be fabricated on any substrate material that is sufficiently smooth for thin-film fabrication and that can withstand temperatures to 250°C. To date, the RSC microrelay has been fabricated on GaAs, epitaxial GaAs, silicon, and quartz substrates. Devices, furthermore, have been fabricated on both standard thickness and thinned substrates. We expect the microrelay can be realized as well on other high performance substrates (such as alumina, gallium nitride and others) of any chosen thickness. For the work performed in this program, GaAs substrates were used exclusively.

shunt metal   drive metal

SiO2

signal-line stack

1. Spin polyimide layer and deposit first metal layer:

6. Etch areas anchoring structure to substrate

2. Spin polyimide layer and deposit second metal layer:

7. Deposit structure oxide:

3. Spin sacrificial polyimide layer:

8. Deposit drive metal:

4. Etch recess defining area of top contact:

9. Pattern structure oxide:

5. Deposit metal for contact shunt:

10. Etch sacrificial polyimide to release structure:

Fig. 3.2: Schematic of MEMS RF switch fabrication process

3.2   RSC Switch Performance

Performance for the RSC microrelay has been characterized over a broad frequency range, from DC to W band. Typical S-parameter data are shown in Figure 3.3 for a microstrip-configuration relay on a semi-insulating GaAs substrate.   Microrelay S-parameters are determined from network analyzer measurements of short-length (~500 um) devices.   Relay isolation in its OFF state is very good (particularly at lower frequencies), with >60dB isolation at low frequencies and ~30dB isolation at 40 GHz. This isolation is mostly limited by electrical coupling through the substrate. Insertion loss for the relay ON state is low over the entire band due to the use of metal contacts. Total device insertion loss is ~0.2-0.3dB from DC to 40 GHz, with ~0.1dB due to the relay contact itself and the remainder due to the conductor losses of the signal line. Return loss (not shown) is also very good, ranging from -40dB at 1 GHz to –25dB at 40 GHz.
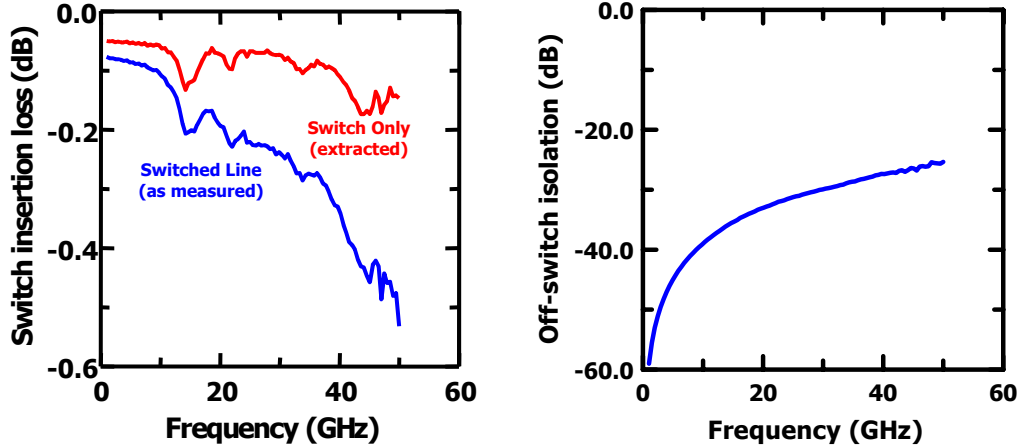
Fig. 3.3: MEMS switch S-Parameter data for device on ON (left) and OFF (right) states.

In addition the RSC microrelay offers excellent RF linearity and electrical isolation between RF signal and DC control lines. Two-tone measurements have been used to characterize relay RF linearity for its conducting state. These two-tone measurements show low intermodulation products with IP3 of +80dBm. The electrical isolation between signal and control lines has been evaluated by modeling. These simulations show isolation of ~50dB between the two conductors.

The electrostatic actuation scheme and mechanical design to great extent determine the microrelay actuation characteristics. Mechanical actuation for the baseline designs typically occurs at ~70 V with low electrical resistance provided by voltages ~20% higher (~85 V). This actuation voltage agrees well with the predictions of mechanical models. Power consumption for actuation is very low, due to the electrostatic actuation mechanism. Switching times are ~10 μs, facilitated by drive capacitor flow holes for the OFF-ON transition and by stiff mechanical springs for the ON-OFF transition.

3.3   *Switch Device Optimization*

Switch performance and form-factor specifications required by the demonstration subcircuit motivated optimization of four key features of the microswitch design. These include:

- *Contact Material* - Switch contact materials migrated from the original Au/Pt metallurgy to Au/Au to reduce contact insertion loss. This halved switch electrical resistance providing more margin and hence device robustness.
- *Contact Geometry* - The upper contact geometry was re-shaped to provide more reproducible insertion loss and enhanced reliability. Initial switch designs utilizing a flat-on-flat contact geometry were modified to a button-on-flat contact.

- *Spring Constant* - The switch mechanical spring constant was increased to minimize sticking failures that impact yield and lifetime. Increases in switch spring constant, however, result in an increased actuation voltage, requiring a performance tradeoff for this design parameter
- *Actuation Voltage* - The electrostatic drive capacitor area was increased to reduce the required actuation voltage. Decreases in spring constant and capacitor gap were unattractive because such changes would reduce mechanical opening forces and make switches more susceptible to sticking failures. This design modification (with additional reliability-driven increases in mechanical spring constant) resulted in a 50% reduction in actuation voltage and improved reproducibility (both device-to-device and wafer-to-wafer)

3.4 *Switch Packaging*

Circuit integration of the MEMS switch required assembly of packaged switch parts that meet the application specifications. This required that the packaging processes not degrade either switch performance or reliability. Second, packaging electrical geometry must provide RF performance suitable for the host circuit. These technology requirements, furthermore, must meet geometry constraints imposed by the test bed. For the filter circuit demonstration, a small sized (0.2 inch square) ceramic package housing 2 MEM switches was selected. Each of these switches (Figure 3.4) is isolated from each other, with discrete RF signal and DC control lines.
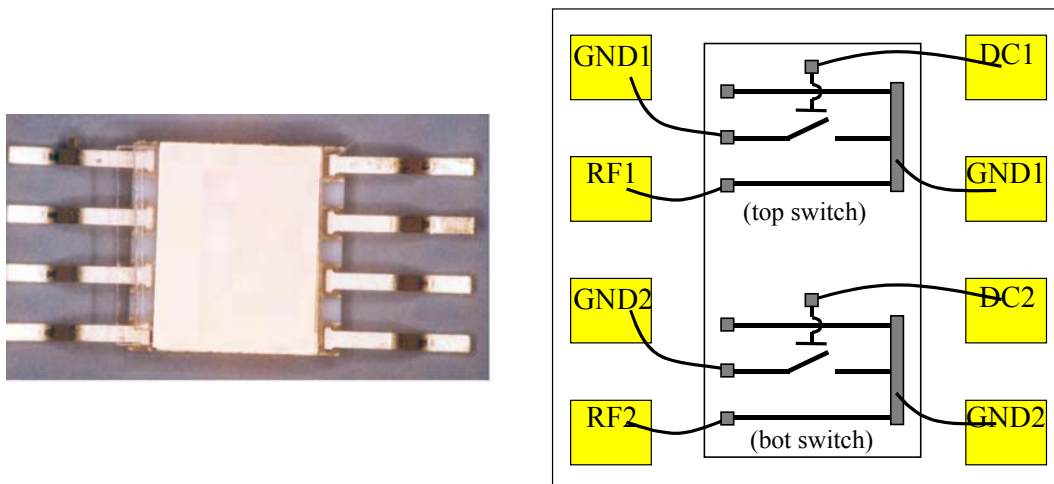
Fig. 3.4: Eight-Pin Package housing MEM switches, and package pinout with electrical schematic of each switch circuit.

Under this program, two development efforts were conducted to optimize the performance of packaged switches. One effort concerned the development of switch/package electrical configurations providing good RF performance. The other effort concerned the development of processes suitable for packaging of switch dies.

3.5 *RF Design of Packaged Switches*

RF design optimizations were required to realize a packaged switch circuit meeting the desired performance specifications. Design changes were developed to minimize RF inductance of the packaged switch circuit. The wirebond electrical connections between package pads and switch die introduce an inductance (a few nH) large enough to adversely impact filter circuit RF performance. This RF inductance of the packaged switch was reduced by two design modifications (Figure 3.5). One change involved redesign of the switch electrical layout, to form a one-port device that switches an input signal to ground. This one-port, grounding configuration eliminates wirebonds to an external ground, nearly halving packaged circuit inductance. The second change involved bonding of two parallel wires to the switch input pad. This double bonding halves again the packaged circuit inductance. The combined design changes provide a four-fold reduction of inductance to a value (0.8nH) acceptable for in-spec circuit performance.
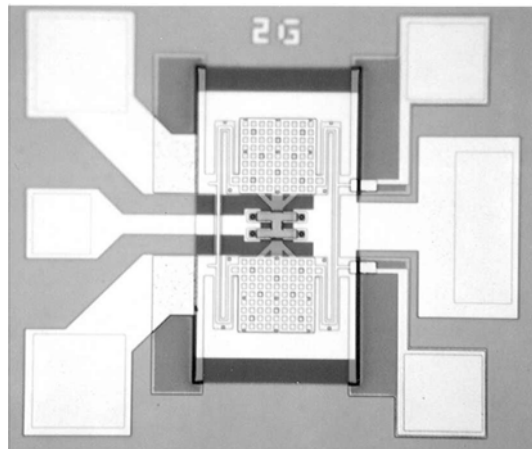
Fig. 3.5:One-Port Grounding Switch layout, with RF input pads at left.

3.6 *Processes for Switch Packaging*

Packaging processes were developed to realize packaged MEM switches preserving switch performance and providing good process yields. This packaging process development addressed all steps of device packaging including singulation of dies from wafers, attaching a die to package, and attaching the lid to seal the package.

3.6.1 *Singulation Process:*
The initial wafer sawing approach for die singulation proved problematic when applied to this application. The problem stems from characteristics of wafer sawing combined with the small die sizes of this application. Wafer sawing is a dirty technique requiring coverage of devices with a protective film, which is removed after sawing. Application of wafer sawing to MEM devices (Figure 3.6) utilizes a process sequence involving deposition of the protection film, sawing into dies, removal of the film, device release, and device testing. This singulation approach, then, requires handling of singulated dies

for three steps. In this application, with very small die size (40mil by 60mil), such extensive handling introduces significant losses from damaged dies.

A scribe-and-break singulation was identified as better approach for this application. Scribe and break is a clean singulation technique involving tape mounting of the wafer, shallow scribing on the wafer frontside, breakage along scribe lines, and tape stretching for die pickup. In particular, no film is needed to protect devices.   Thus, application of scribe-and-break to MEMS devices (Figure 3.6) permits wafer-level release of devices, wafer-level device testing, and singulation of known-good dies.   This sequence minimizes handling of released dies to one step, reducing handling-related losses. Indeed, scribe-and-break yields in excess of 95% were achieved for the application parts.
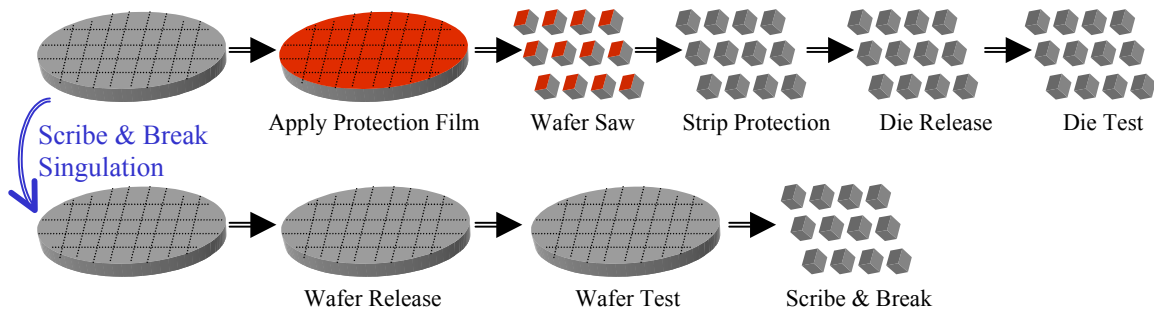
Fig. 3.6: Packaging sequences for initial wafer-saw singulation process (top) and optimized scribe-and-break singulation process (bottom).

3.6.2   Die and Lid Attach Processes:

Evaluations of traditional die and lid attach processes proved them to be detrimental to MEM switch performance.   Initial attachment experiments investigated epoxy and thermoplastic adhesives, processes traditionally used for electronic circuit applications. These experiments, involving before-and-after testing of switches on bonded dies, showed significant increases in the electrical resistance of switches after attachment. This electrical resistance increase, furthermore, could not be reversed under any thermal treatments. This performance degradation is believed to stem from adhesive vapors, which condense onto switch contacts and introduce a surface-film resistance.

Alternative die/lid attach processes, offering better compatibility with the MEM switch, were identified and demonstrated. Best results were achieved for attachment based on reflow of fluxless eutectic solders. The fluxless eutectic solder process allows bonding of dies using low-temperature heating and with materials providing minimal vapors. Attachment experiments using such alloys showed that microswitch performance is unaffected by the bonding process.

3.7   *Packaged* *Part* *Characterization*

The optimized switch and package technology developed under this program showed an electrical response that achieves the required packaged-device performance requirements derived from the circuit specifications.   Switch insertion loss was determined from S Parameter measurements of packaged switch circuits.   These S-parameter measurements were fit to an electrical model of the packaged part, with switch insertion loss as a fit variable.   A packaged switch model with fit parameters, for a typical device is shown in Figure 3.7.   Switches exhibit an insertion loss of <1Ohm at application frequencies.

Switch speed was determined from oscilloscope transient measurements for DC signals. This oscilloscope measurement involves single-trigger mode signal capture of the voltage across the switch when it is toggled by a step-function drive. Typical switch speed curves, for both OFF-ON and ON-OFF transitions, show that switch response settles within ~10usec, with minimal bounce events.   This switch time is within the 15usec required for this application

Package Model   Switch Model
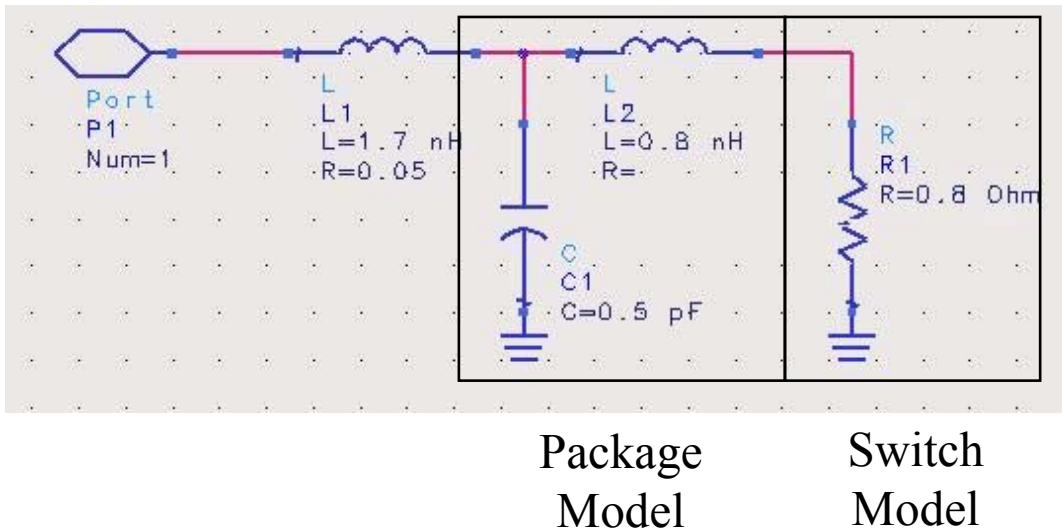
Fig. 3.7: Fitted electrical model of packaged switch in its ON-state, with switch showing 0.8 Ohm resistance.
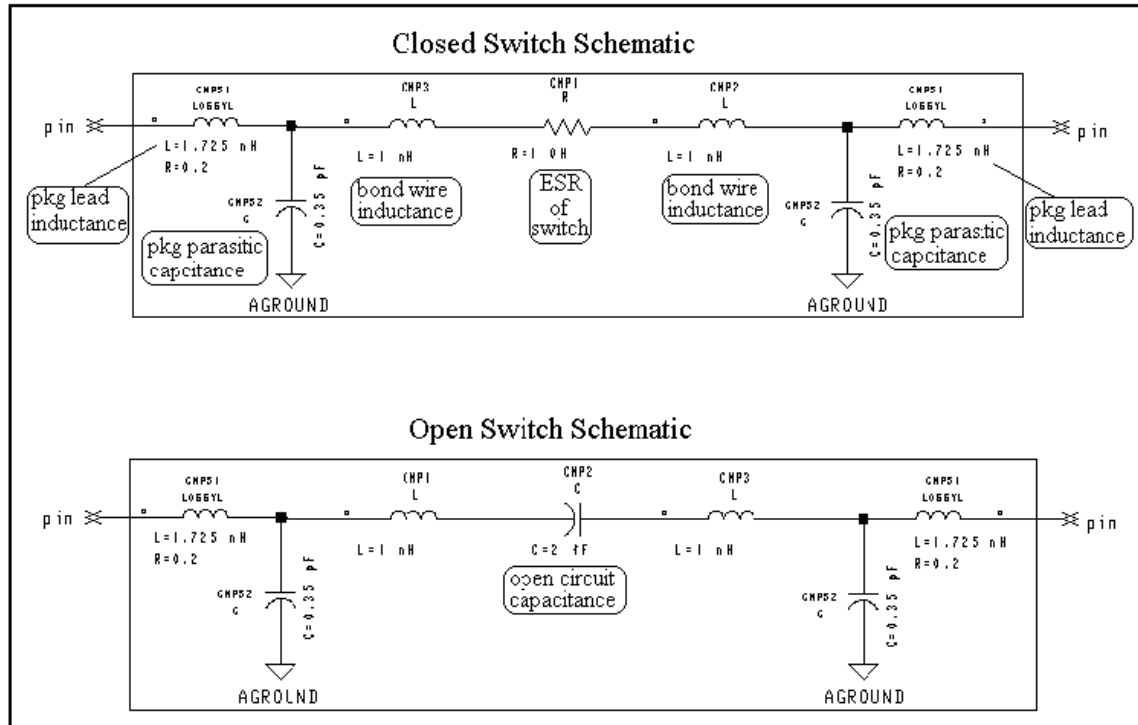
Fig. 3.8: Detailed electrical model of packaged switch in open and closed states.

4 MEMS Tunable Capacitor Device Development

Solid-state tunable capacitors, such as varactor diodes, typically have limited tuning ranges, high insertion loss, poor electrical isolation, and significant nonlinearity. This can impose substantial complexity to RF circuitry in order to compensate for these limitations in high-performance tunable filter applications. For example, wide tuning range filters implemented with traditional semiconductor varactor diodes can require complex series-parallel circuit constructions to achieve sufficient signal linearity. The MEMS tunable capacitors, by contrast, function by the physical dimension changes of MEMS actuators, permitting high linearity while preserving broad tunability.

There have been a number of different implementations of MEMS tunable capacitors presented in the literature. The majority of these have used the electrostatic vertical deflection of a suspended parallel plate, varying the air gap dimension to achieve the capacitance tuning. Due to the inherent electrostatic instability, this approach is typically limited to capacitance tuning ranges of less than 50% [4.1], and is expected to be susceptible to significant signal nonlinearities from high effective RF voltages, especially near the limit of their stable tuning range. Alternate techniques to increase the stable tuning range have been demonstrated, such as use of parallel plate devices with dissimilar drive and RF gap dimensions [4.2], digitally-selectable two-state sub-elements [4.3], and active drive feedback. Under the efforts conducted in this program, we have focused instead on lateral drive capacitors to achieve wide tuning range and tactically-relevant

13

base capacitance values with simple control circuitry. The development of the device technology has been described in detail in a number of publications [4.1, 4.4, 4.5].

The wide tuning range application of the F-22 UHF filter imposes challenging performance specifications on the MEMS device. These circuit performance requirements have been flowed down to the device level, and the derived component requirements for the packaged tunable capacitor are:

- Capacitance Range: 2.5 - 10 pF (4:1)
- Tuning Voltage Range: 1-6 VDC desired, can accommodate up to 28V
- Max series resistance: 1.0 Ohm @ 10 pF
- $I_{RF,}$ V_{RF} (op): 0.18 A, 21 V RMS respectively
- Tune Time: 10 usec max.

4.1 *Baseline Device Concept*

The basic device construction pursued under this program has been a lateral drive tunable capacitor based on an array of interdigitated combs, Fig. 4.1. The capacitance tuning is achieved by mechanically varying the degree of insertion of the movable comb "fingers" relative to the stationary combs. To first order (neglecting fringing fields), the overlap area of the combs determines the capacitance. To achieve high specific capacitance (capacitance per unit die area), narrow gaps and large comb depths are desired. Thus, a fabrication approach based on Si deep-etch processing is preferred over surface micromachining technologies.

The construction of the device uses separate drive and signal combs, with the actuation provided by electrostatic attraction of the drive combs. This lateral comb drive approach avoids the electrostatic instability of vertical-drive parallel plate capacitors and permits continuous analog tuning over a large capacitance range. The use of electrostatic actuation enables operation with extremely low control power. Using this architecture, the base capacitance of the device can be easily adjusted by varying the number of comb fingers.
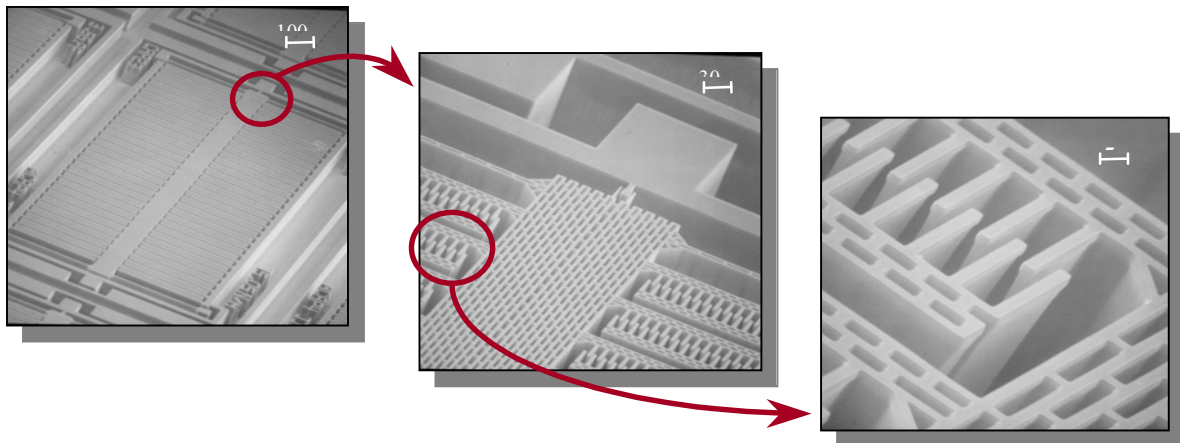
Fig. 4.1: Micrographs illustrating RSC MEM Tunable Capacitor

The construction of the device used a 3-terminal implementation approach, shown schematically in Fig. 4.2. Here, separate tuning capacitors and RF signal capacitors sharing a common ground terminal are used. This avoids the need for large biasing inductors to isolate the RF signal from the tuning voltage. Since the drive and signal capacitors are mechanically linked, the mechanical motions generated by the tuning capacitor translate directly into a capacitance change in the RF signal path. This enables independent design of the drive and signal elements of the device for optimum performance.
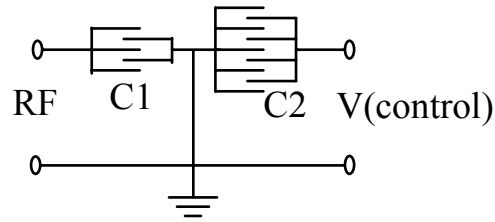
Fig. 4.2: Schematic of electrical configuration of MEMS tunable capacitor

The original fabrication methodology for the tunable capacitor devices was based on a Silicon on Insulator (SOI) process. Here, a 20 micron thick Si device layer was originally used for the tunable capacitor device, with the buried oxide layer serving as both the etch stop and sacrificial layer, Fig. 4.3.
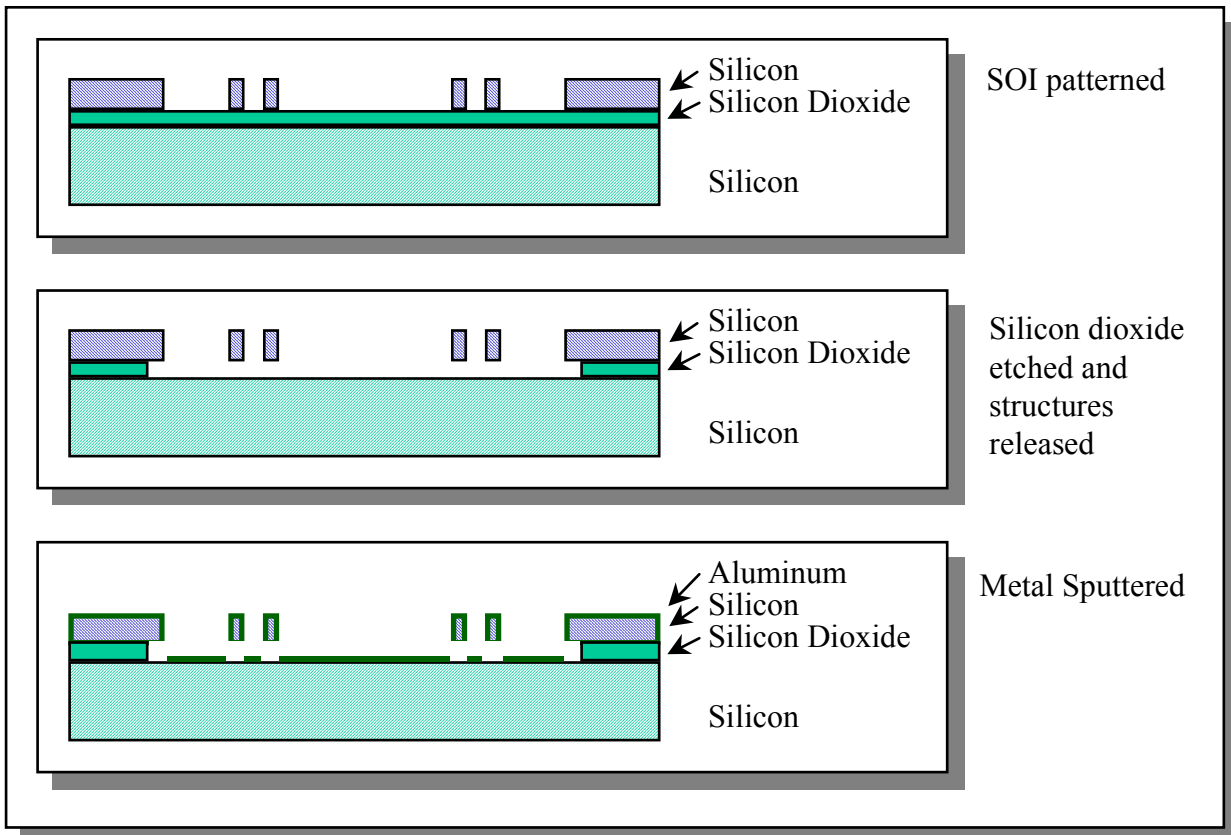
Fig. 4.3: Schematic process flow of original tunable capacitor approach

15

The Tunable Capacitor structures were fabricated in this SOI process using a Deep Reactive Ion Etch (DRIE) procedure. This process was attractive for its simplicity, requiring only a single mask level of processing. A key requirement in its execution is the ability to generate high aspect ratio, deep etch features at small spatial dimensions. The deep etch enables a larger capacitance per unit die area to be achieved through increased overlap area. The high aspect ratio etch profiles enable small separations between combs to be achieved, also resulting in a high base capacitance. The original device designs (shown in Fig. 4.1) utilized 2 μm wide comb fingers with 2 μm separation. The etch depth for these structures was initially in the range of 20-28 μm, although this was increased in later device generations. The release procedure on the initial SOI-based devices was performed using a standard supercritical CO_2 extraction technique.

Initial measurements on the SOI tunable capacitor validated the mechanical characteristics of the device. Under an applied voltage, the relative degree of insertion of the comb fingers could be controllably varied. For the initial structures, the overlap of these fingers could be varied by approximately a factor of 3 for an applied voltage of 15V, Fig. 4.4. For these initial structures, the untuned base capacitance values were between 1.78-3.28 pF depending on design. Preliminary RF characterization of the MEMS tunable capacitor validated the tuning characteristics of this device, with experimental results closely matching those derived by finite element modeling of the design.
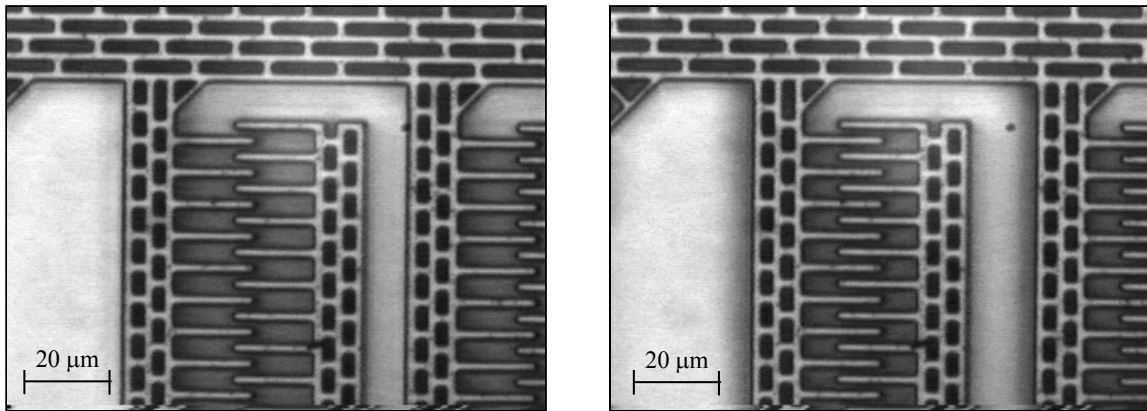
Fig. 4.4: Optical micrograph of Tunable Capacitor device in an unbiased state (left) and at a bias voltage of 15 V (right). Note increase in comb finger overlap at an applied voltage.

4.2 *Device Refinement – Reduced Parasitics*

The optimal performance of the tunable capacitor device in the tunable filter circuits requires wide tuning range and highly capacitive response characteristics. This in turn requires reduction in the capacitive and inductive parasitic contributions. Developmental efforts were conducted throughout the course of this program to mitigate these factors, addressing contributions from both substrate and bond pad effects.

4.2.1 Substrate Parasitics:

The initial 1-mask SOI process and supercritical CO_2 release resulted in a capacitor structure electrically isolated from, but in close proximity to, the underlying silicon substrate. In this geometry, the post-release metalization resulted in a significant degree of conductive structure on the Si substrate that coupled strongly with the RF capacitors. This configuration presented a large parasitic effect in the RF performance of the tunable capacitor. Figure 4.5(a) illustrates this effect using S11 in a Smith chart for a frequency sweep from 30 MHz to 2 GHz. The overall shape, along with the small, local resonant loops, is a clear indication of the unwanted parasitic interactions. Based on this observation, processing modifications were implemented to remove the portion of the silicon substrate directly underneath the tunable capacitor with a second masking step to minimize the substrate coupling. Dramatic improvements were achieved as shown in Fig. 4.5(b), which is a S11 plot for a frequency sweep from 30 MHz to 6 GHz. This improved tunable capacitor exhibits a near-ideal capacitive behavior with an electrical self-resonance as high as 5 GHz. A schematic process flow for this device is shown in Fig. 4.6.

(a)   *(b)*
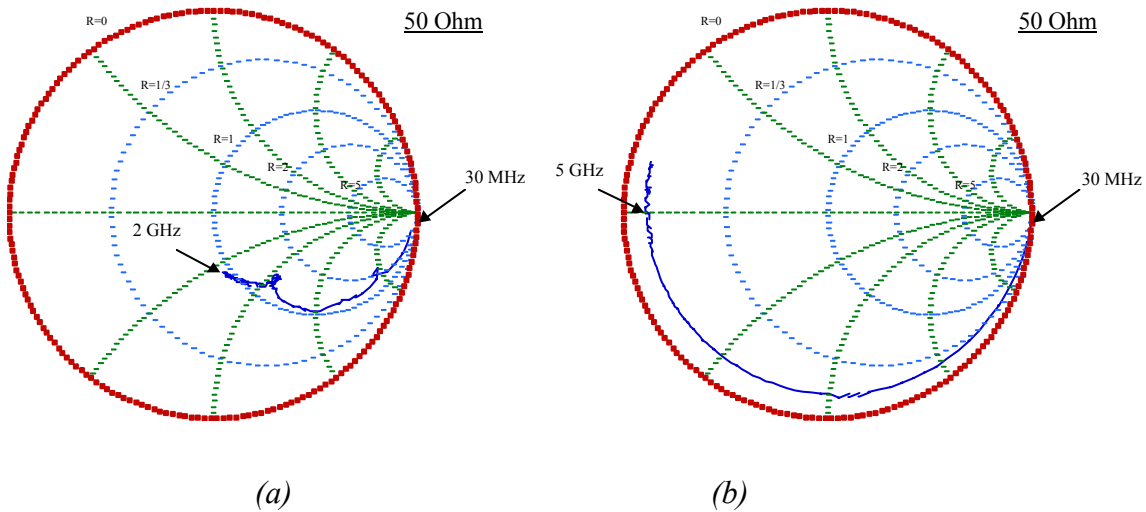
Fig. 4.5: S11 plots showing (a) strong parasitic effects with silicon substrate intact, and (b) minimal parasitic effects with portions of the silicon substrate removed.
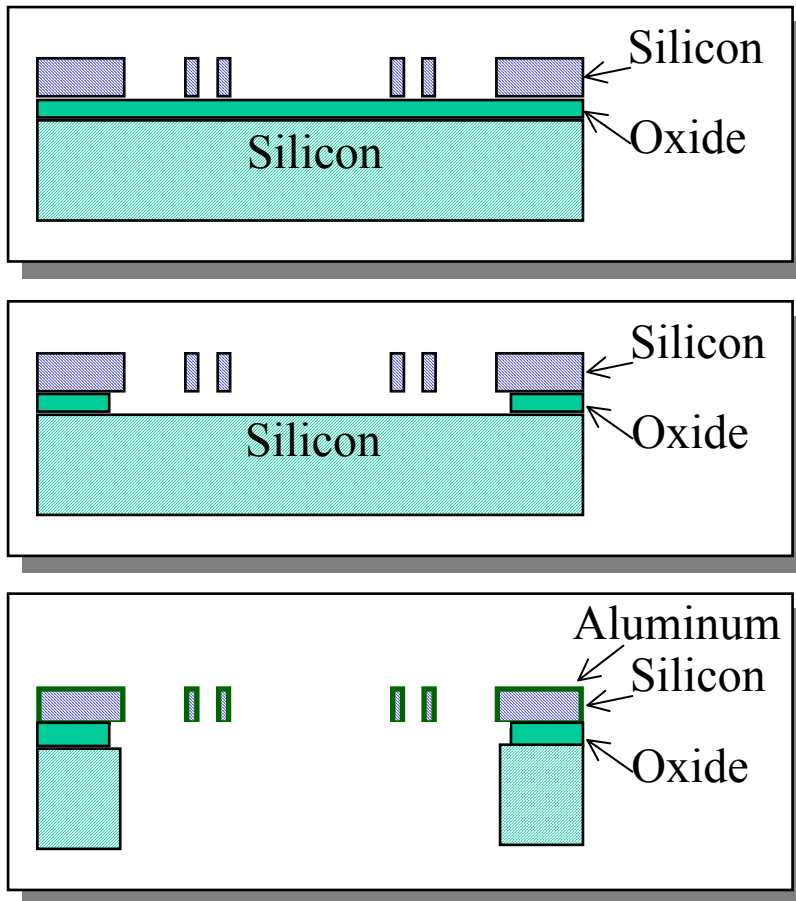
Fig. 4.6: Schematic process flow for substrate-removed tunable capacitor process designed for reduced substrate parasitics.

The substrate-removed device achieved wide tuning range (in excess of 3:1 for this particular sample) and low tuning voltage, offering substantial benefits for the intended system insertions. Theoretical modeling of the device tuning response showed it to be well behaved, with the measured capacitance as a function of voltage agreeing closely with the theoretical calculations.

4.2.2 Bond Pad Parasitics:

The removal of the substrate underneath the capacitor resulted in significant reduction in coupling interactions to the substrate. An additional contribution was also identified arising from coupling to the silicon substrate beneath the mechanical anchors and bond pads. This effect had not been observed in the earlier wafer-probed measurements due to the measurement calibration to the probe points. The observed data was consistent with a significant loss through the low-resistivity Si handle substrate and resulted in a significant added (fixed) capacitance. This large fixed capacitance led to a significant reduction in the net capacitance tuning range for packaged and wire bonded parts

To address the reduction of this parasitic component in the tunable capacitor, two potential avenues for process modification to the device were explored:

- Silicon-on-Insulator (SOI) using high resistivity Si for the supporting substrate
- Silicon-on-Glass (SOG) to eliminate through-substrate conduction

The SOG process was expected to provide better RF characteristics, but at the expense of a larger perturbation to the original process flow.

To quantify the contributions of the bondpad structures and assess the benefits of the proposed solutions, simpler, non-movable test structures were fabricated. These fixed capacitors had none of the interdigitated finger structures of the MEMS structure, and provided a means of isolating and quantifying the contributions of the anchor/bondpad structure. These patterns were applied to 10 Ohm-cm and 4000 Ohm-cm silicon substrates, as well as on glass substrates for evaluation of parasitic effects seen on the previously fabricated tunable capacitors.

Results of the comparative RF measurements for the different substrates showed that the glass samples had minimal parasitic effects as expected, and the 4000 Ohm-cm silicon samples had a much-reduced parasitic capacitance compared with the original 10-20 Ohm-cm samples. A best fit to the measured s-parameter data was performed to extract the effective substrate parasitic capacitance for the various substrate materials, as summarized in Table 4.1.

Table 4.1: Summary of substrate capacitance contributions from data fit

Substrate	Extracted Fixed Capacitance
12.5 Ohm-cm Si	2.05 pF
4000 Ohm-cm Si	0.212 pF
Glass	0.0825 pF

Initial test samples of the tunable capacitor on high-resistivity Si were conducted to validate these experiments. This approach utilized an SOI process, identical to the original process flow but using custom SOI starting material with a high resistivity carrier wafer (>4000 ohm-cm). The process sequence included the substrate removal under the interdigitated comb region to reduce parasitic coupling after metallization. For the initial demonstration devices, metallization involved Al sputtering, with about 0.5 microns applied from both the top side and bottom side of the structure. While this thickness resulted in higher series resistance than ultimately desired, it still provided a mechanism for assessing parasitic capacitive contributions.

RF measurements were made on the high-resistivity Si devices to assess the static capacitance and tuning behavior relative to theoretical predictions. Wafer-probe data showed significant reduction in the parasitic contribution and good capacitive behavior in the zero-voltage and voltage-tuned states, Fig. 4.7. The nominal capacitance value from the measurement as a function of voltage is shown in Fig. 4.8.

4.8 GHz   6 GHz   30 MHz   **3.2 GHz**   6 GHz   30 MHz

V = 0 V   V = 13 V

(3.32 pf)   (6.36 pf)
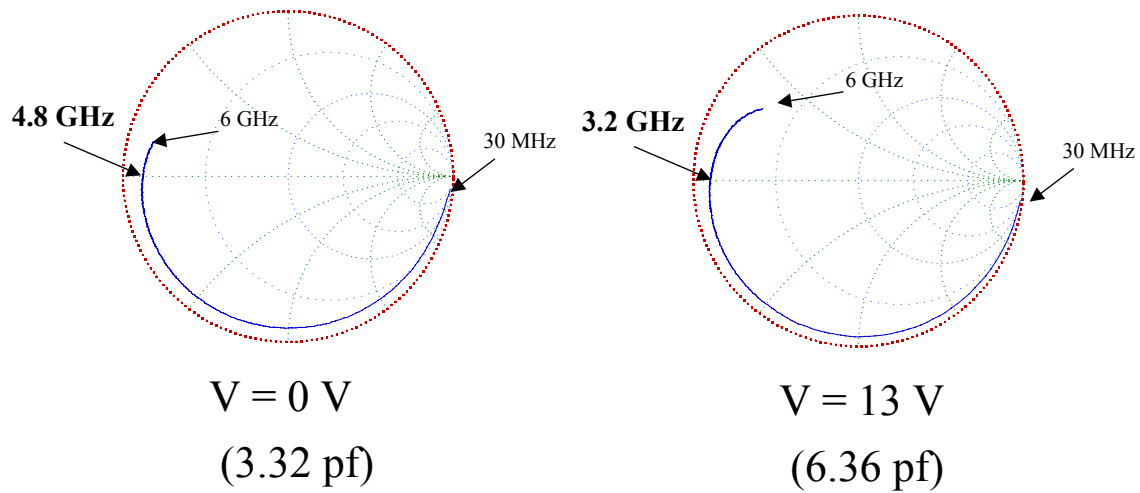
Fig. 4.7: Measured RF performance of tunable capacitor on high-resistivity Si in zero-voltage and voltage-tuned states.
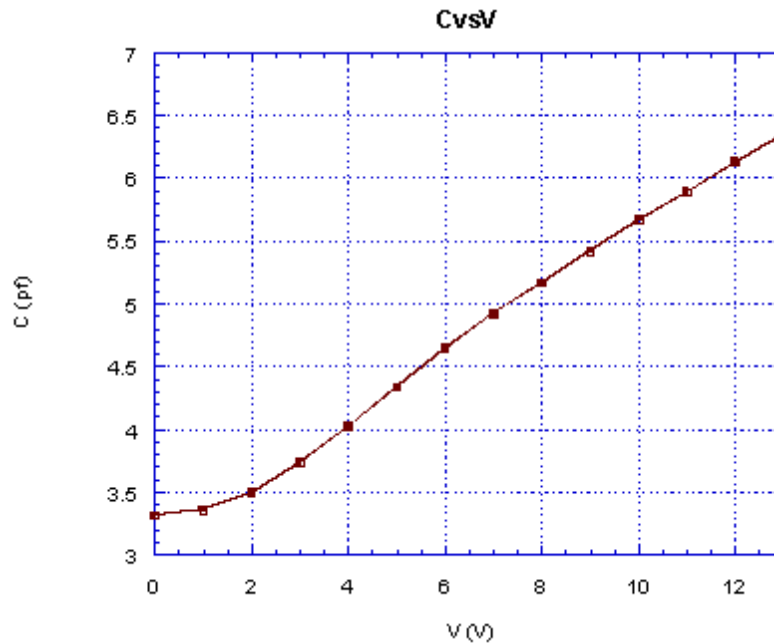
Fig. 4.8: Nominal capacitance reading from network analyzer as a function of applied voltage for tunable capacitor on high resistivity Si.

A packaged sample of this high-resistivity tunable capacitor was compared to a device of identical structural design fabricated on low-resistivity Si. This comparison showed a significant reduction in parasitic capacitance achieved by the higher substrate resistivity, Fig. 4.9. The capacitance difference between the two devices was approximately 1.8pF,

closely matching what had been predicted from theoretical modeling and preliminary experiments.
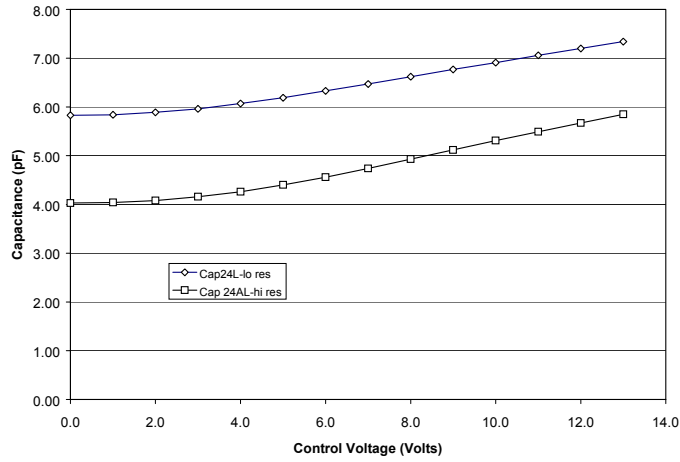
Fig. 4.9: Measured capacitance (100MHz) as a function of tuning voltage for low-resistivity (top) and high-resistivity (bottom) carrier wafers.

4.3   Refined Fabrication Process

Based on the substrate comparisons, it was decided to transition the tunable capacitor fabrication to a Si on glass (SOG) process for reduced parasitics. This was necessary to achieve the >4:1 net capacitance tuning ratio required for the device once wire bonded and packaged. The process flow for device fabrication was modified to accommodate the glass substrate, Fig. 4.10. The use of a low-temperature epoxy bond to join the Si and Glass wafers provided a larger separation between the two device layers, enabling frontside metallization of the released device without compromising RF performance.
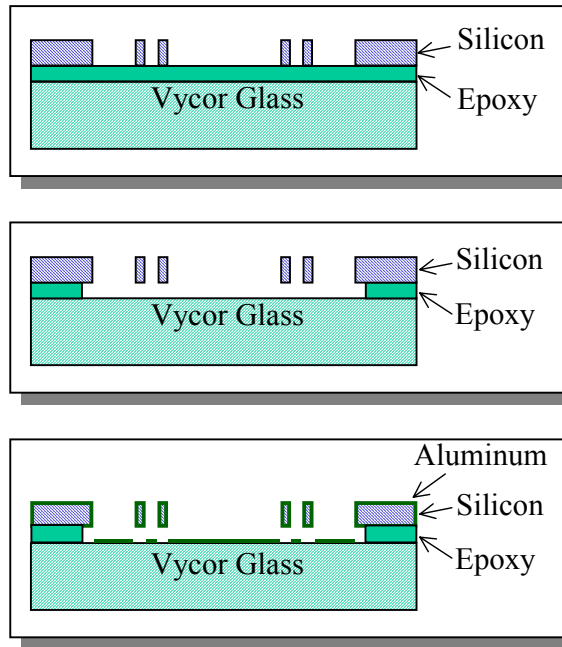
Fig. 4.10: Schematic process flow for SOG implementation of tunable capacitor

Devices were fabricated in the SOG process, and showed wide tuning range and highly capacitive response characteristics. When fully engaged with a 16 μm overlap between the interdigitated comb fingers separated by 3 μm gaps, the initial SOG tunable capacitor test device had a maximum capacitance of 4 pf with minimal parasitics. The Smith chart of Fig. 4.11 shows a frequency sweep of this device from 30 MHz to 6 GHz. Tests of other device structures have similarly validated the improvements in tuning ratio and base capacitance enabled by the reduced substrate losses, Fig. 4.12
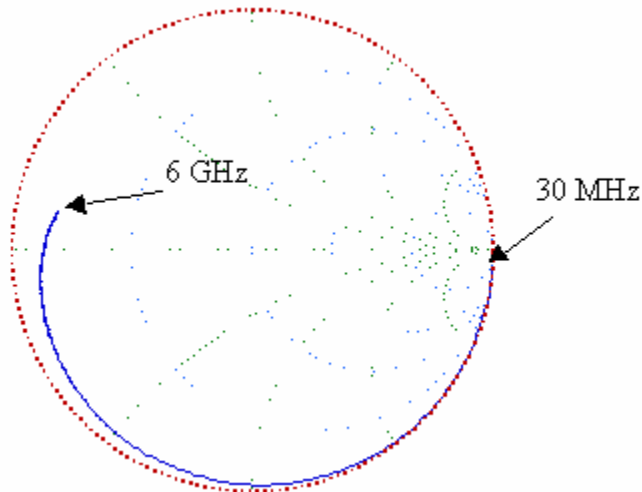
Fig. 4.11: S11 plot (30 MHz to 6 GHz) of the tunable capacitor tested with 0.75 mm of Al deposited on the side-walls of the single crystal silicon device. Vycor was used as the substrate.
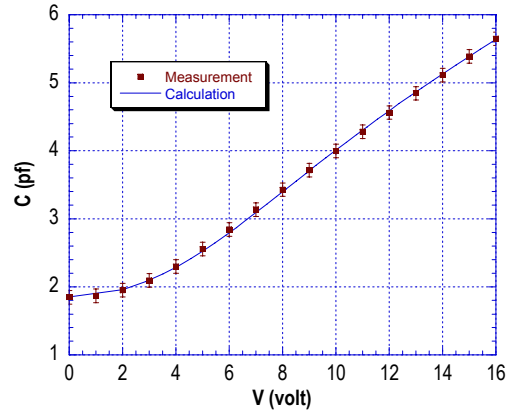
Fig. 4.12: Measured capacitance vs. voltage behavior for tunable capacitor

4.4 *Improved Device Performance*

The SOG process addressed the reduction in device parasitics necessary for tuning range extension in packaged parts. Additional device refinement was necessary to achieve the flowdown specifications for the filter circuit. These included increased electrical Q (for filter loss requirements) higher breakdown voltages (to enable increased mechanical stiffness) and greater tuning range to accommodate package parasitics and still maintain net tuning range >4:1. Refinements to the design and process were implemented which resulted in improvements in both electrical and mechanical metrics. These included:

- Modified suspensions for reduced series resistance and decreased sensitivity to vibration. Previous research showed that a large portion of the resistance loss for movable structures is associated with the thin mechanical suspensions. Therefore, new device designs with thicker suspension were implemented. In past designs, any device with a suspension greater than 3 μm in width was unable to achieve the full motion needed for a 4x tuning ratio. However, using a new double suspension design in which each end of the device has two suspensions of equal width, devices were successfully fabricated with suspensions as large as 6 μm in effective width. A double 3 μm suspension reduces the series resistance by 30% over a standard 2 μm suspension.
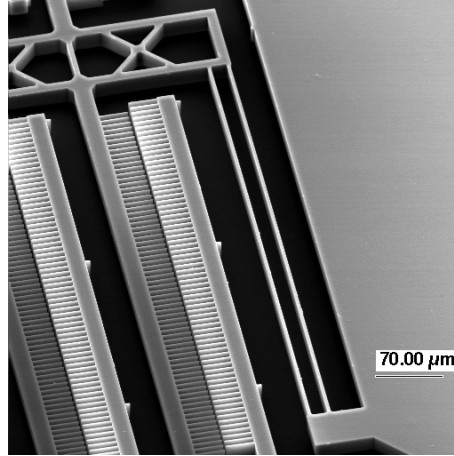
Fig. 4.13: SEM of a new double beam suspension that allows wider suspensions to still achieve large displacements.

Several advances in vibration immunity were achieved for the tunable capacitor. The new, thicker suspension designs that reduced the series resistance of the device also achieved increased resonant frequencies. The stiffer suspensions increased the resonant frequency by over 300% relative to the earlier, softer flexures. In addition to stiffening up the device, the total mass of the suspended structure was decreased by hollowing out the arms of the device. This created an additional 25% increase in the resonant frequency of the device.

- Use of a low resistivity (0.005-0.02 $\Omega*cm$) device layer, and a thicker device layer (40 microns). This has further reduced the series resistance another 30-50% over standard resistivity silicon devices. The thicker device layer reduced the relative contribution from the parasitic components, resulting in an increased tuning ratio. The use of thicker device layers had the added benefit of increasing the base capacitance to levels closer to the target 2pF value. In addition, because the total capacitance scales linearly with the device thickness, a smaller device area could now be used for the capacitance range needed for this application. To date, tunable capacitors with device layers up to 80 μm have been successfully fabricated.

- Two-sided metalization to counterbalance the mismatch stress, reducing the out-of-plane bending from 4.5μm to 0.2 μm. This allowed a thick metal layer to be deposited without degrading planarity. In this process, metal layers can be patterned on both sides of the silicon device layer to reduce the out-of-plane bending caused by CTE mismatches between the silicon and metal layers. Prior to bonding, aluminum is patterned on the bottom side of the silicon device layer. Using a through device layer etch of alignment marks, a 0.5 μm alignment tolerance can be achieved between the top and bottom metal pattern. After the device has been released, additional metal can be sputtered onto the structure to increase device Q.

These modifications resulted in an exceptionally large tuning range, larger than 8.4 to 1, Fig. 4.14

.

Capacitor Tuning Range
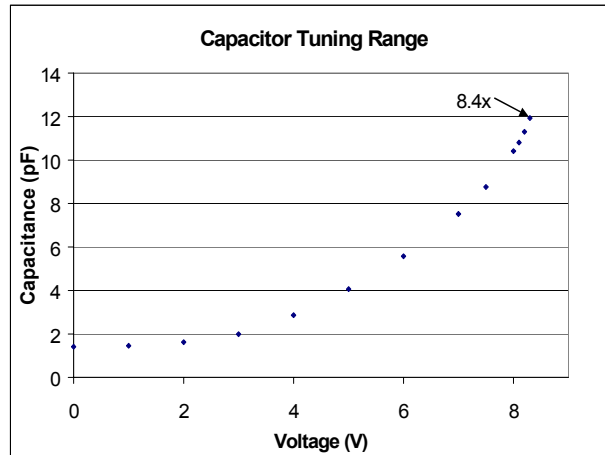
Fig. 4.14: Tuning range of the device measured at 500 MHz.

These modifications reduced the series resistance to less than 1 Ω with corresponding increase in device Q. Figures 4.15 and 4.16 show the S11 parameters and the device Q at the minimum capacitance. The device has a low parasitic effect and is not near self-resonance out to a frequency of 3 GHz. The device also has a Q above 100 out to 700 MHz, making it ideal for the tunable filter application in the 200 – 400 MHz range for which that the device was designed.
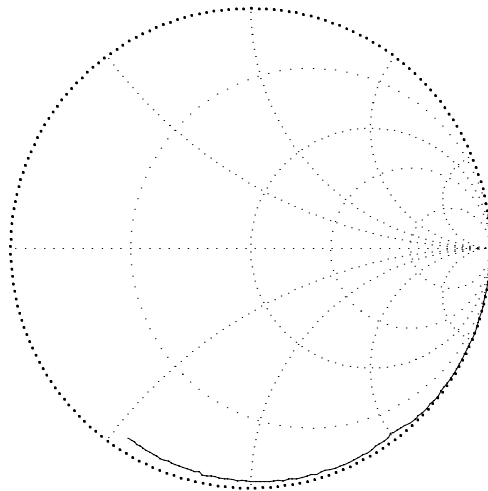
Fig. 4.15: S11 plot of the device from 100 MHz to 3 GHz with no actuation and a capacitance of 1.5 pf.
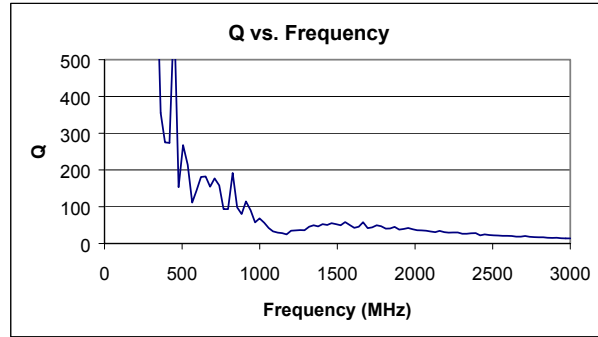
Fig. 4.16: Quality factor of the device from 300 MHz to 3 GHz with no actuation and a capacitance of 1.5 pf.

Figures 4.17 and 4.18 show the S11 parameters and the device Q at the maximum capacitance. The increased capacitance reduces the self-resonance down to around 2 GHz. In addition, the Q factor is reduced, but remains above 100 up to 200 MHz, the intended operation frequency at the 8 pf capacitance range.
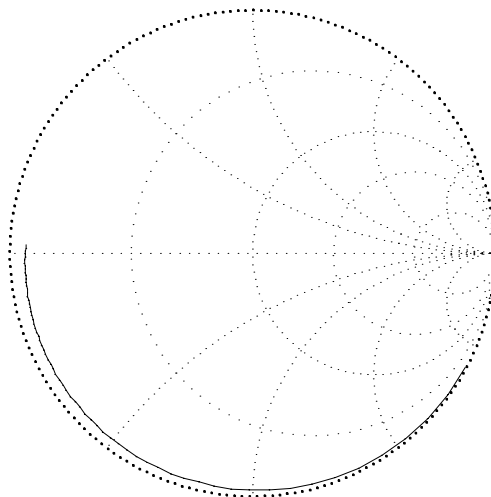
Fig. 4.17: S11 plot of the device from 100 MHz to 2 GHz with an actuation voltage of 7 V and an 8 pf capacitance at 200 MHz.
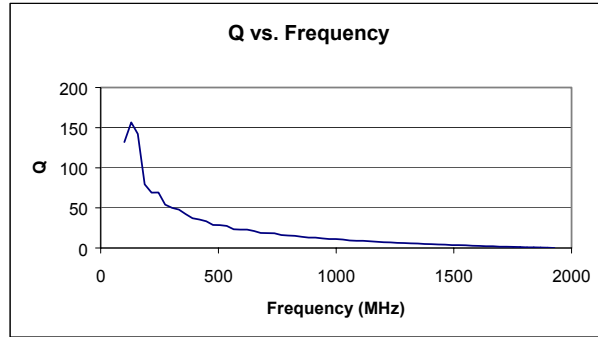
Fig. 4.18: Quality factor of the device from 100 MHz to 2 GHz with an actuation voltage of 7 V and a capacitance of 8 pf at 200 MHz.

To achieve more accuracy in the series resistance measurement, characterization in a resonant test fixture was performed on a small number of MEMS variable capacitors. These devices had fairly low series equivalent resistance and more than 4:1 capacitance range as indicated by small-signal S-parameter measurements. The resonant fixture places the capacitor in a series-resonant, low loss transmission line resonator in shunt on a 50 Ohm through-transmission line. At resonance the resonator induces a large reduction (notch) in signal transmission on the through-line. By measuring the notch frequency and depth and numerically correcting for the inherent fixture loss and reactive loading, the capacitance and equivalent series resistance of the MEMS capacitor can be determined. Typical device resonant fixture results (Table 4.2) show high Q (exceeding specification) at low tuning voltage (low capacitance) but somewhat lower than desired Q at high voltage (high capacitance). A 225 MHz Q value of more than 80 at maximum capacitance is needed for the 2-pole UHF filter demonstrator to meet low-end center frequency insertion loss specifications.

Table 4.2. MEMS Capacitor Capacitance and Q versus Frequency and Tuning Voltage

Tuning Voltage (Volts)	Measurement Freq. (MHz)	Capacitance (pF)	Q-Factor
0	208.105	1.58	125
0	403.475	1.62	111
5	177.000	6.0	65.2
5	304.225	6.26	37.1

Incorporating both of these design changes, series resistances below 1 Ohm have been achieved, meeting the specification for the tracking filter application over the full operational range. The Q is above 100 in the 200-400 MHz range for which this device is intended to operate. The Smith chart for this device is shown in Figure 4.19, illustrating the clean capacitive response and negligible parasitics.

27
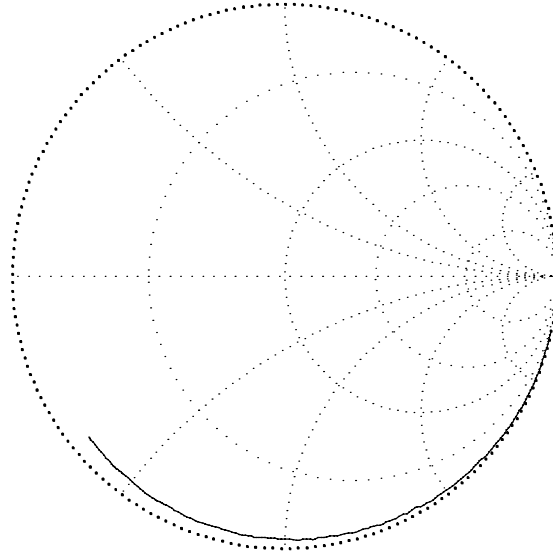
Fig. 4.19: Smith chart for a high Q tunable capacitor.

At program completion, devices had achieved record tuning range, with a measured range as high as 11.9x with smooth mechanical operation in the 2-8pF capacitance range targeted for the filter application. Devices optimized for low resistance achieved series resistance below 0.77 Ohm at 400 MHz, meeting the <1 Ohm series resistance specification for the F22 filter application. Measurements of this device at Collins has shown device Q values in the range of 70-200.

4.5   *Device Packaging*

The tunable capacitor devices were packaged in ceramic packages for filter integration. Due to the absence of contacting surfaces, the tunable capacitor had much more flexibility in package process selection as compared with the RF switch. Here, epoxy die attach and thermoplasic lid seals could be used without degrading device performance. Package models were extracted to support filter circuit design, Fig. 4.20
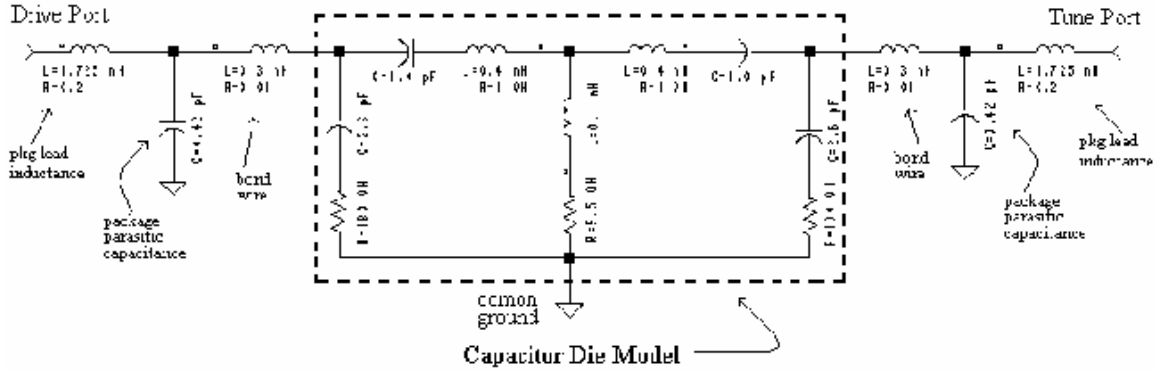
Fig. 4.20: Package model for tunable capacitor

4.6   *Tunable Capacitor Lifetime Testing*

The long-term reliability of MEMS devices is an issue that is often raised due to the periodic stress conditions inherent to mechanical motion. To address the question for the tunable capacitor device, we have conducted initial lifetime tests to evaluate any degradation or changes in properties associated with operation for a large number of cycles. Due to the single crystal silicon construction of the device and its purely elastic flexure regime, it would be expected to be quite resistant to mechanical fatigue effects. Further, the absence of contacting surfaces would be expected to make it less prone to environmental reliability factors.

The device was operated in an oscillatory mode, excited at its resonant frequency. This allowed operation at increased levels of deflection (to represent worst-case stresses) and helped shorten the test duration. The frequency of operation was 3.787 kHz, as determined visually by maximum oscillatory amplitude. Tests were run on a device packaged in ambient lab atmosphere.

The device was operated continuously for more than 10 billion cycles with no apparent effects on mechanical or electrical performance. The resonant frequency of the device was unchanged, indicating no detectable alteration of flexure mechanical properties. These results are consistent with literature observations of the durability of single-crystal MEMS devices. Similar measurements of the C vs. V performance over the life of the test showed no change in tuning response characteristics, Fig. 4.21, 4.22.
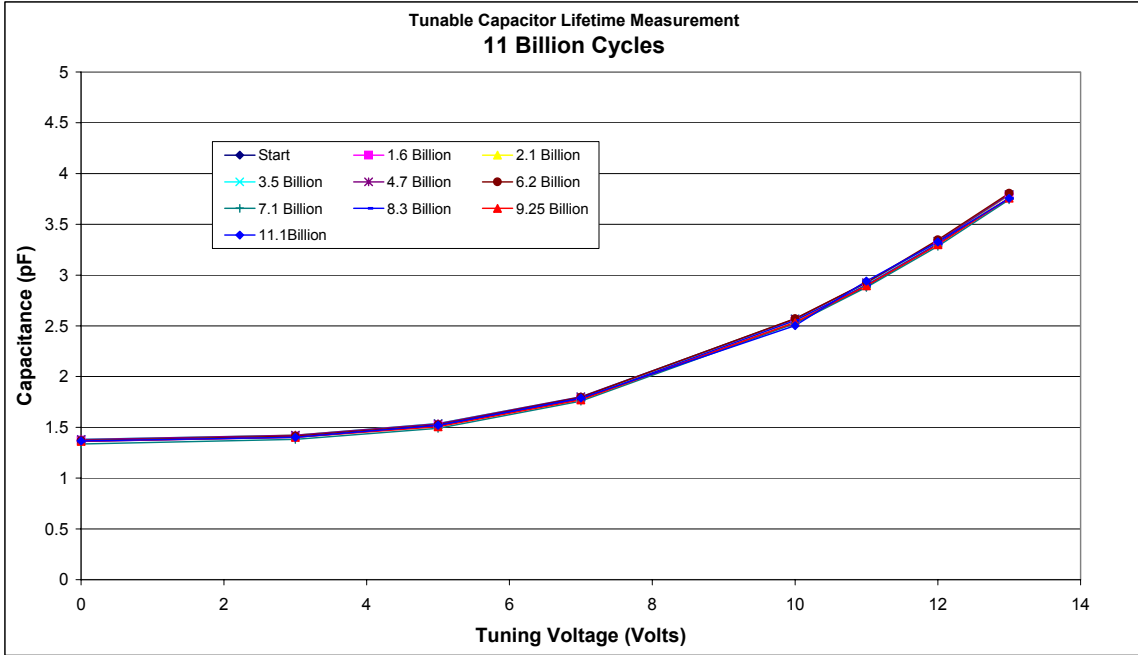
Fig. 4.21: Capacitance vs. voltage response of MEMS tunable capacitor device before and after 10B cycles of operation
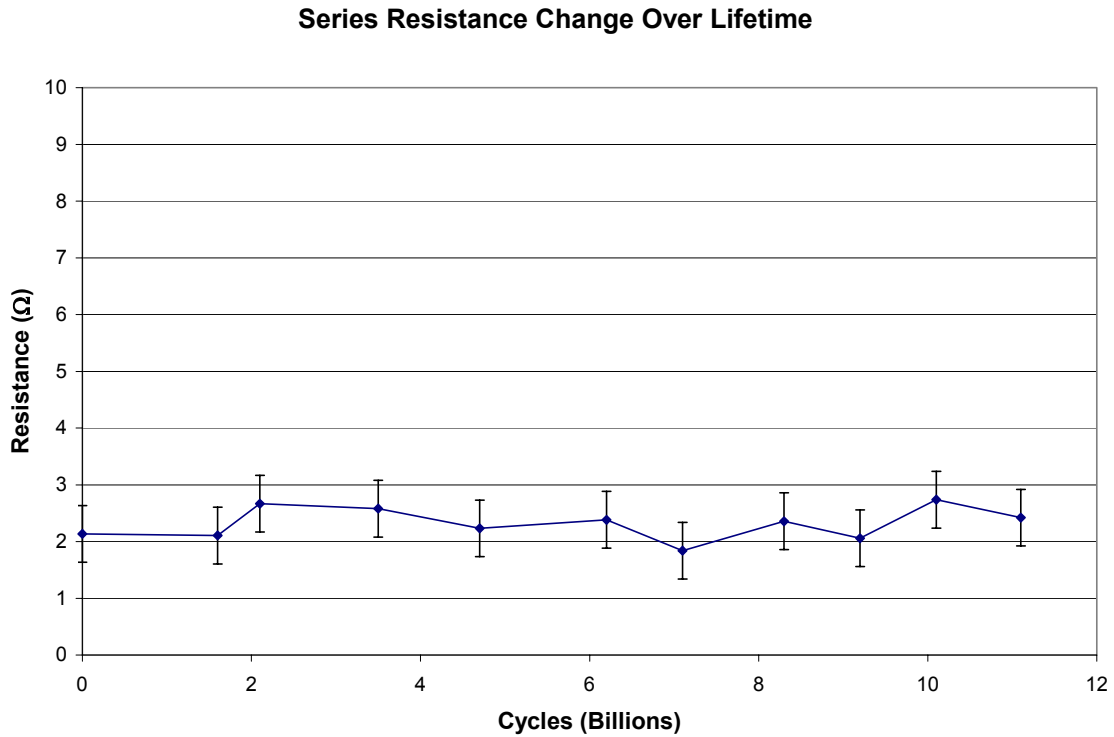
Fig. 4.22: Change in series resistance over time for a tunable capacitor. Variations are within experimental error

5   MEMS Switch-Based Filter Insertion

5.1   *Switch-Based Tunable Filter Circuit*

The demonstration vehicle for the switch-based tunable filter demonstration was the VHF midband preselector filter for the RA-66 (Comanche) Helicopter Antenna Interface Unit (AIU). The present circuit uses PIN diodes to switch discrete capacitors in order to accomplish the filter tuning, Fig. 5.1. The Comanche RAH-66 Antenna Interface Unit (AIU) uses a 6-pole filter constructed from 3 two-pole filters. Under this program, the demonstrations were limited to the two-pole subassemblies
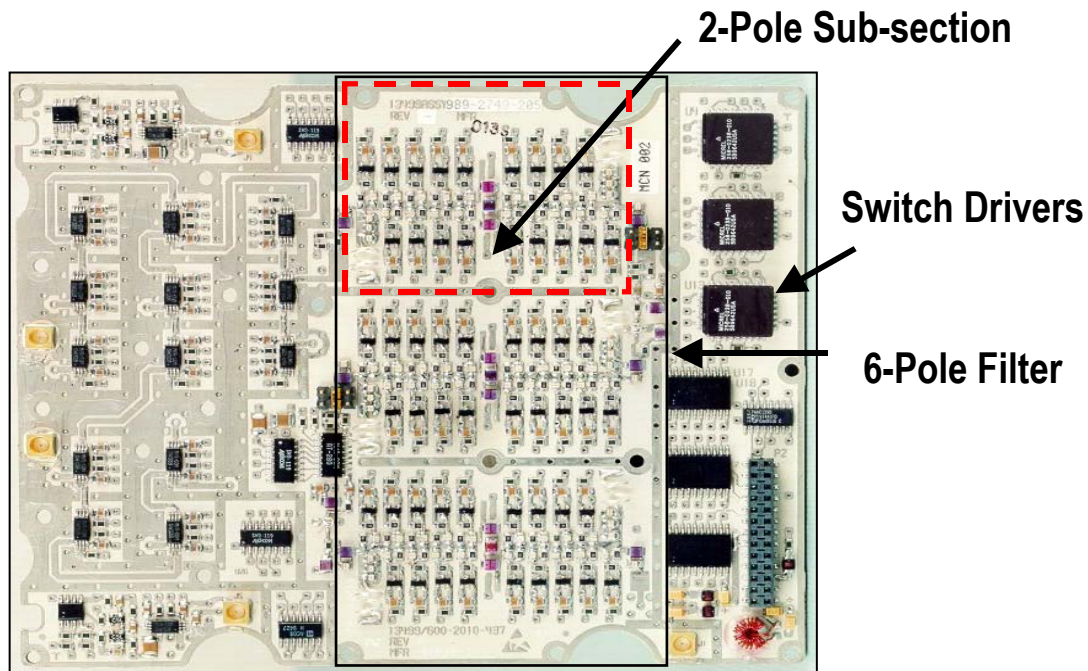
Fig. 5.1: Photograph of PIN-based 6-pole filter assembly

The specifications of the RAH-66 (Comanche) AIU sub-assembly 2-Pole VHF filter include:

- VHF Step-tuned Bandpass Filter 116-152 MHz
- Center Freq. Tuning Range: 116-151.975 MHz
- Selectivity (fo ±8 MHz) ≥ 13.4 dB rejection
- Tune time: < 75 microseconds
- 2-pole midband loss < 4.5 dB
- 2-pole 1 dB compression pt. > +20 dBm

For the MEMS-based equivalent filter, the PIN diodes were replaced with MEMS switches. The goals of this demonstration were to achieve increased dynamic range and reduced parts count relative to the existing PIN-based circuit

5.2 *MEMS-Based Circuit Design and Fabrication:*

A MEMS-based circuit was designed to accomplish the filter tuning characteristics. The subcircuit consists of two arrays of 8-switched capacitors to ground, with passive components coupling RF signals between the arrays. The subcircuit hardware consists of a RF fixture with discrete MEM switches in packages and the capacitors as surface-mount components. Each package is a small sized (0.2 inch square) ceramic package housing 2 MEM switches. Each of these switches is isolated from each other; with discrete RF signal and DC control lines. A schematic of the two-pole filter circuit is shown in Fig. 5.2.
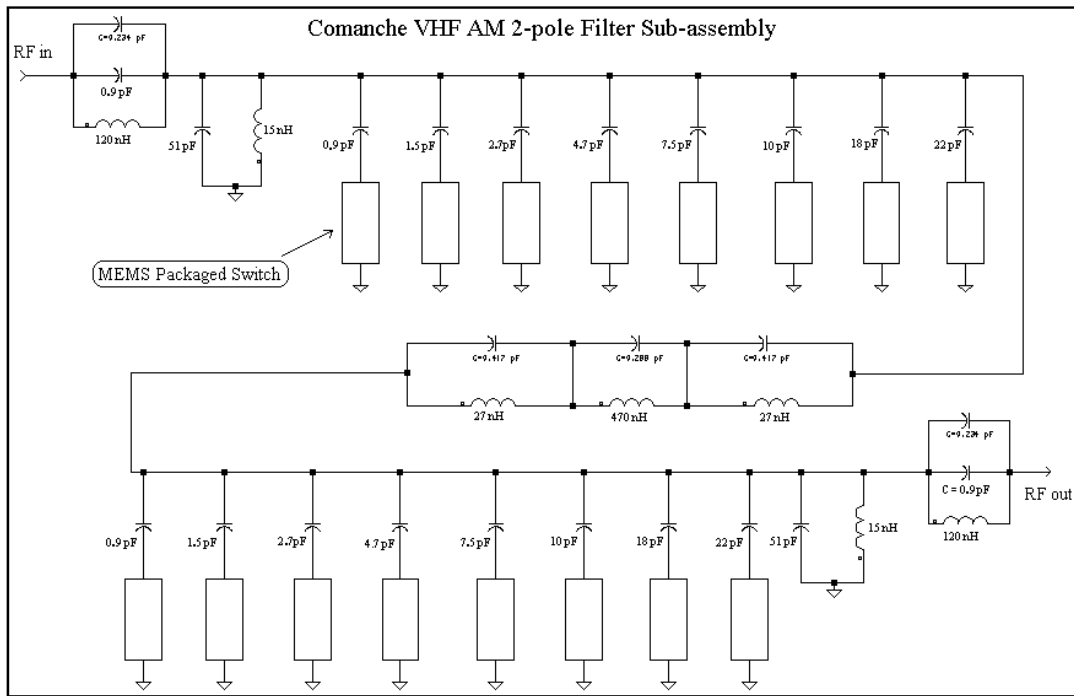
Fig. 5.2: Schematic of two-pole tunable VHF filter circuit using MEMS RF switches and fixed capacitors.

MDS simulation of the preliminary filter design was conducted to evaluate the effects of switch resistance on filter bandwidth, Fig. 5.3. These simulations indicated that a significant reduction in bandwidth was associated with reducing the switch resistance from 6 Ω to 2 Ω. For further reductions below 2 Ω, however, only marginal improvements in filter response were realized. From this, a target resistance of below 2 Ω has been established for the RF Switch. This value was consistent with measured device performance.
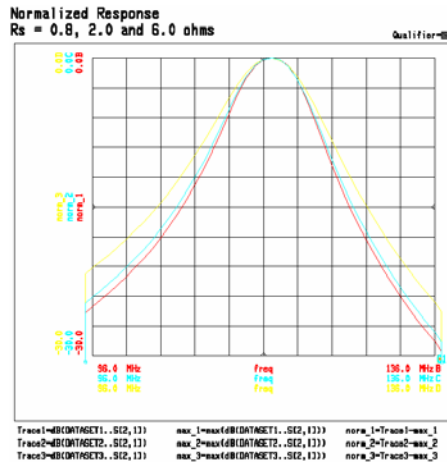
Fig. 5.3: MDS Simulation of preliminary tracking filter design, showing effect of RF Switch resistance on filter bandwidth.

The filter circuit has been implemented using packaged MEMS switch devices. The MEMS switches were fabricated in a coplanar waveguide (CPW) geometry with a grounding switch configuration. Two switches were incorporated in each package. A photograph of the two-pole filter is shown in Fig. 5.4. No efforts were taken to miniaturize the initial circuits.

Packaged MEMS Switches
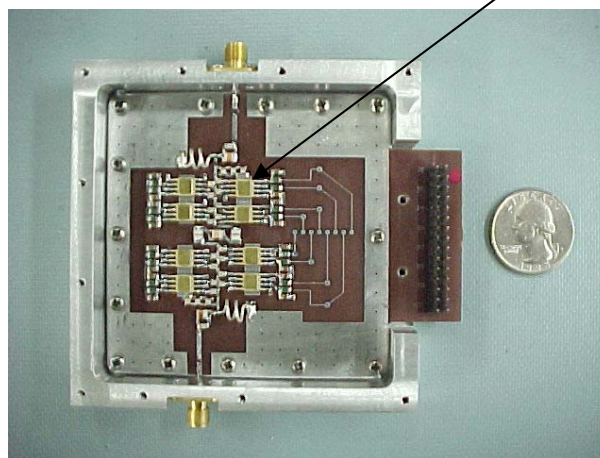
Fig. 5.4: Prototype two-pole tunable filter assembly

5.3 _MEMS-Switch Based Filter Testing_

Measurements of the filter transmission as a function of frequency were made for the different MEMS switch configurations. These demonstrated the ability to tune the filter over the full frequency range of interest while maintaining good filter characteristics, Fig. 5.5
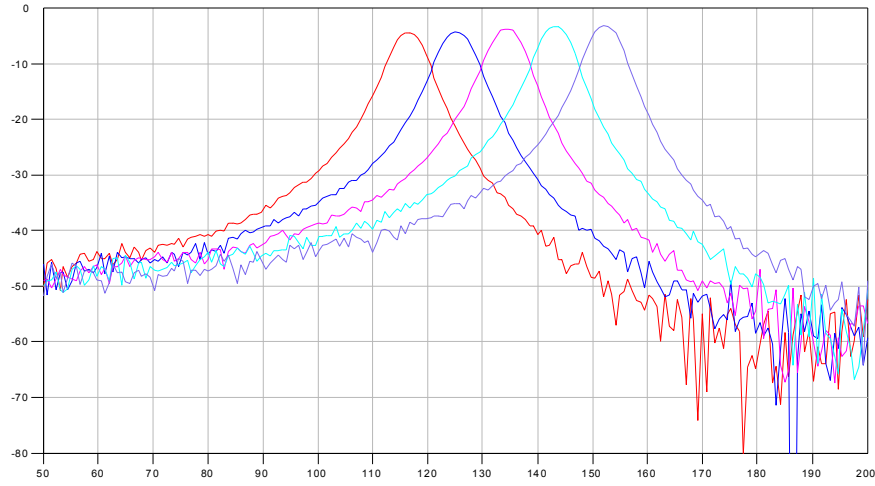
Fig. 5.5: Measured loss as a function of frequency for the two-pole tunable filter circuit. Limited number of filter states shown for clarity

Measurements of the filter characteristics across the tuning range were made to quantify circuit performance. The MEMS–based filter was below the center frequency loss specification of 4.5dB over the full tuning range, Fig. 5.6. Similarly, the filter bandwidth was nearly constant at 3.5MHz over this range, translating to a percent bandwidth of between 2.3% and 3%, meeting bandwidth specifications (Fig. 5.6).
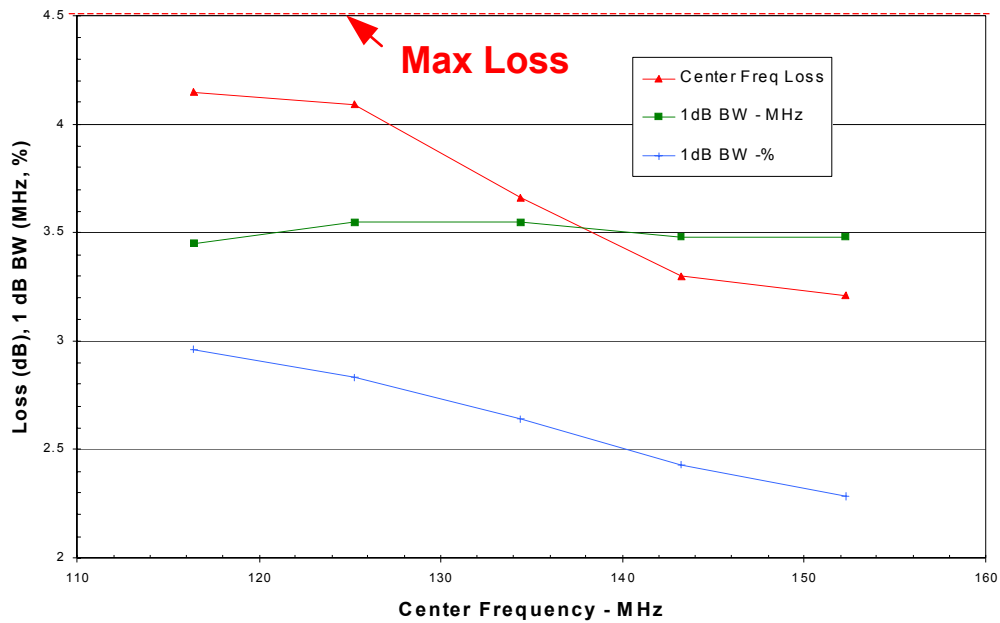
Fig. 5.6: Measured filter performance as a function of center frequency for MEMS tunable filter circuit. Shown are center frequency loss, absolute bandwidth and percent bandwidth. Maximum center frequency loss spec shown for reference.

Filter rejection characteristics were also measured across the tuning range. These were evaluated at +/- 8MHz, +/- 26MHz and +/- 53MHz from center frequency. In all cases, the MEMS-based filter exceed the application rejection specifications, Fig. 5.7.

2-Pole MEMS Switched-Cap VHF Filter
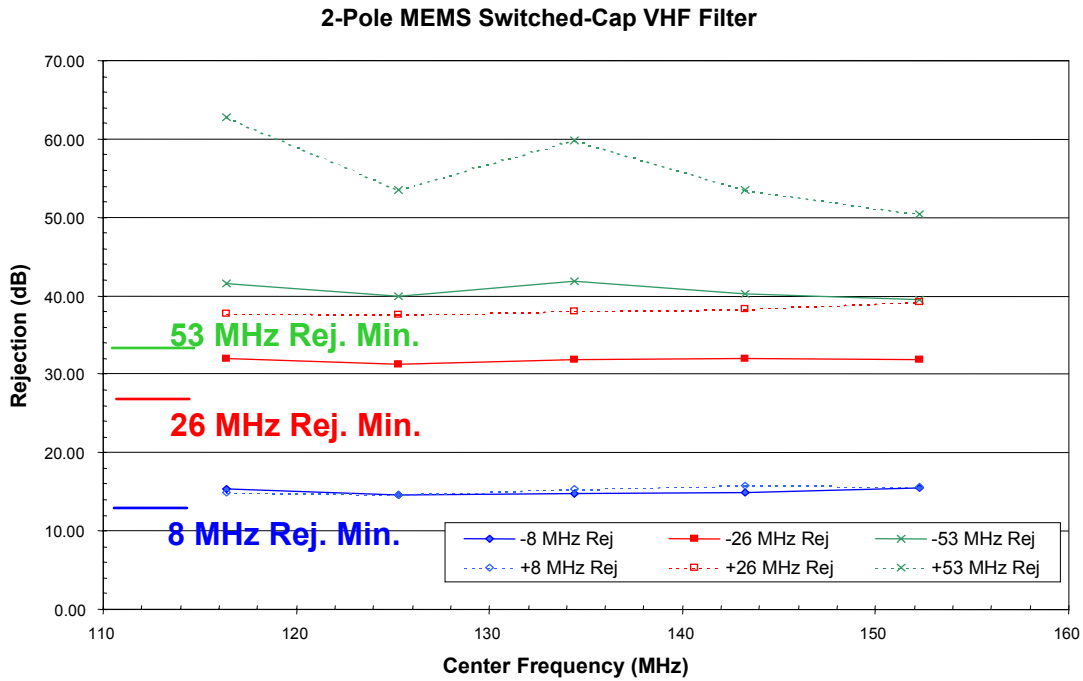
*Fig. 5.7: Measured and target values of filter rejection at +/- 8, 26,
and 53MHz from center frequency across filter tuning range*

Of particular interest was the initial measurement of filter linearity, which was performed using a two-tone method in which two single-frequency tones are applied and the intensity of intermodulation products measured. These tests utilized two RF tones separated by 200kHz. Significant amounts of RF power (+20dBm per tone) were required in these tests to produce measurable intermodulation products, Fig. 5.8. The measurements indicated an IP3 value of approximately +55.75 dBm under these test conditions. For comparison, the equivalent assembly based on PIN diode switches had an IP3 of approximately +28dBm. This 500x improvement in linearity can potentially translate into significant simplifications in the circuit and further parts count reduction.
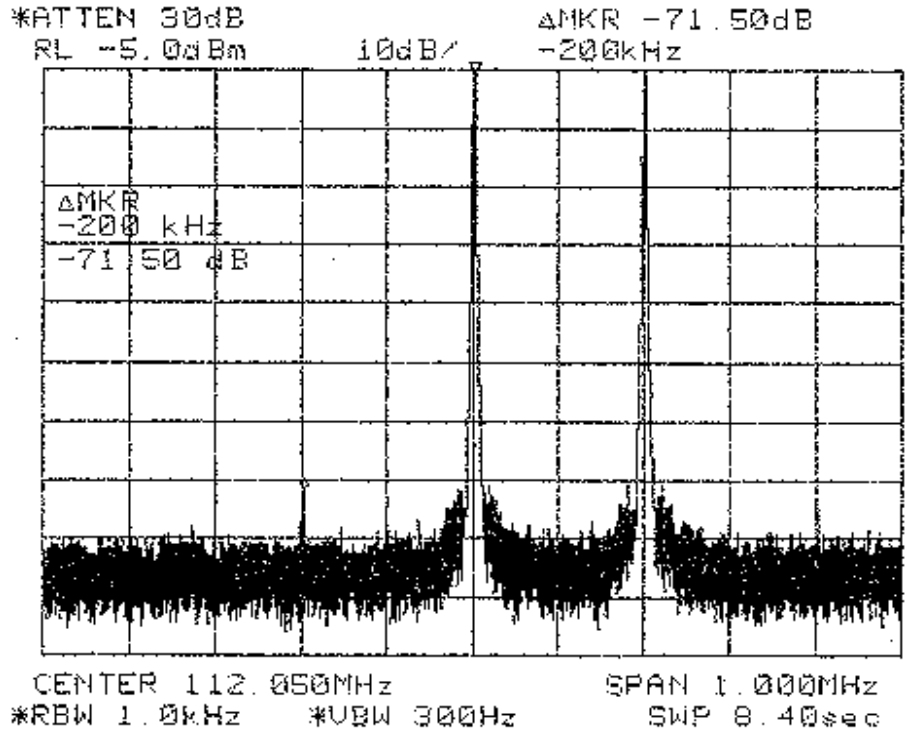
Fig. 5.8: Measured intermodulation characteristics of prototype 2-pole filter. Output tone level +20dBm, IMR3 = -71.5dBc, $IP3_0$ - +55.75dBm

A summary of the switch-based filter performance is given in Table 5.1.

Table 5.1: summary of measured performance of MEMS-based two-pole filter circuit and corresponding diode-based circuit.

	Diode-based design	MEMS-based design
Rejection:	Meets req'ts	Meets req'ts
Passband Loss	Meets req'ts	Meets req'ts
Tune Speed	Meets req'ts	Meets req'ts
Intercept Pt.	+30 dBm	**+55 dBm**
Parts Count:	123 parts/2-pole (369 parts/6-pole)	**71 parts**/2-pole (213 parts/6-pole)
Filter Current Consumption:	~100 mA (max) /2-pole (~300 mA (max)/6-pole)	**~0 mA**/2-pole* (~0 mA/6-pole)*
DC Power:	**~**1.5 W/6-pole	~**0 W**/6-pole*

(*Note: Current consumption and DC power results for the MEMS-based design reflect the quiescent power required to drive the switches.)

The prototype MEMS-based filter met all RF specifications for this tactical communications application. These demonstrations clearly validated the utility of the

MEMS switch for RF filter applications, and highlighted two key benefits offered by the MEMS: linearity (which would be critical for cosite mitigation) and power consumption (which would critical for weight constrained applications). Present limitations of this technology are associated with cycle reliability and power handling capability.

5.4 *Compact Filter Demonstrations*

Extensions of the switched capacitor bank circuit were implemented to demonstrate the size reduction benefits offered by MEMS technology. This involved monolithic integration of the MEMS switches with on-chip capacitors to achieve a single-chip switched capacitor bank circuit. This chip was successfully validated, Fig. 5.9, although we did not yet pursue its integration into the filter circuit.

Fig. 5.9: Compact MEMS-based switchable capacitor bank implemented with on-chip MIM capacitors

6 MEMS Tunable Capacitor-Based Filter Insertion

6.1 *F-22 Filter Assembly*

The demonstration circuit for the Tunable Capacitor device was a UHF voltage-tuned bandpass filter for the F-22 (Raptor) AIU. The characteristics of this 2-pole UHF filter are:

> −UHF Voltage-tuned Bandpass Filter 225-400 MHz
> −Center Freq.Tuning Range: 225-399.975 MHz
> −Selectivity (fo ±13 MHz) ≥ 10.75 dB rejection
> −Tune time: < 27 microseconds
> −2-pole midband loss < 5.5 dB

In the present embodiment of this circuit, the tuning is achieved using semiconductor varactor diodes. A schematic of the present varactor-based circuit is shown in Fig. 6.1. The tracking filter slice of the AIU and the varactor array modules are shown in Fig. 6.2. The complexity of the varactor array is clearly apparent. Further, it is notable that the thickness of the tracking filter slice is defined in great extent by these varactor modules, Fig. 6.3, and that simplification of these circuits could enable significant volume savings in the tracking filter assembly.
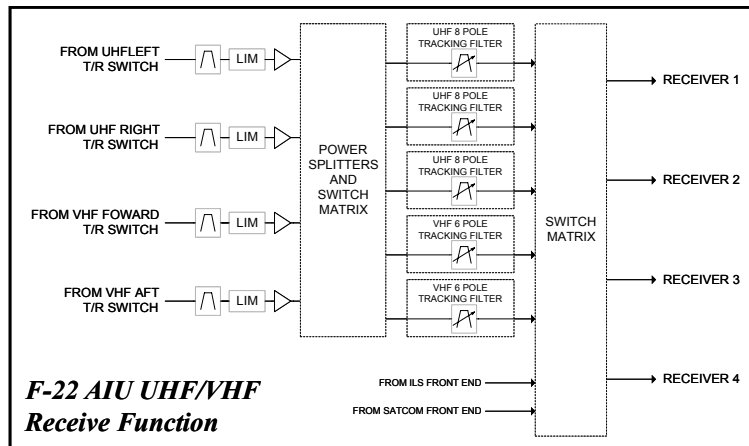
Fig. 6.1: Schematic of F-22 AIU receiver architecture

UHF Tracking Filter

Two Pole Filter   Two Pole Filter   Two Pole Filter   Two Pole Filter

2 Pole Filter

Input   Output

Diode Array   Diode Array

Capacitor Connection

Capacitance Tuning Range 5 to 25 pF

Tune Voltage Input
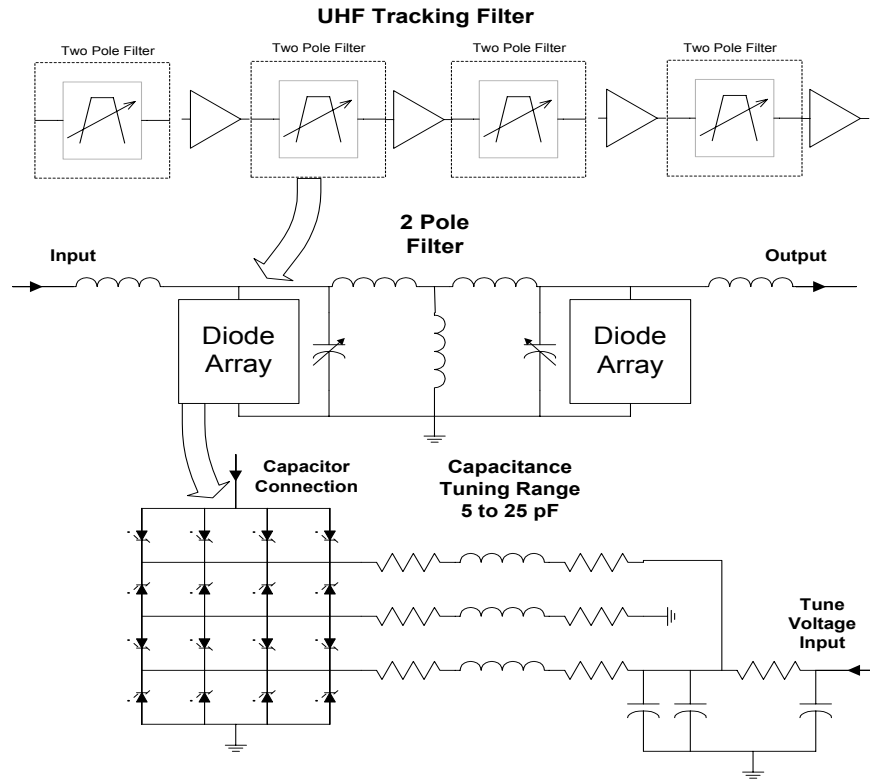
Fig. 6.2: Schematic of F-22 AIU UHF tracking filter, 2-pole filter, and varactor diode assembly
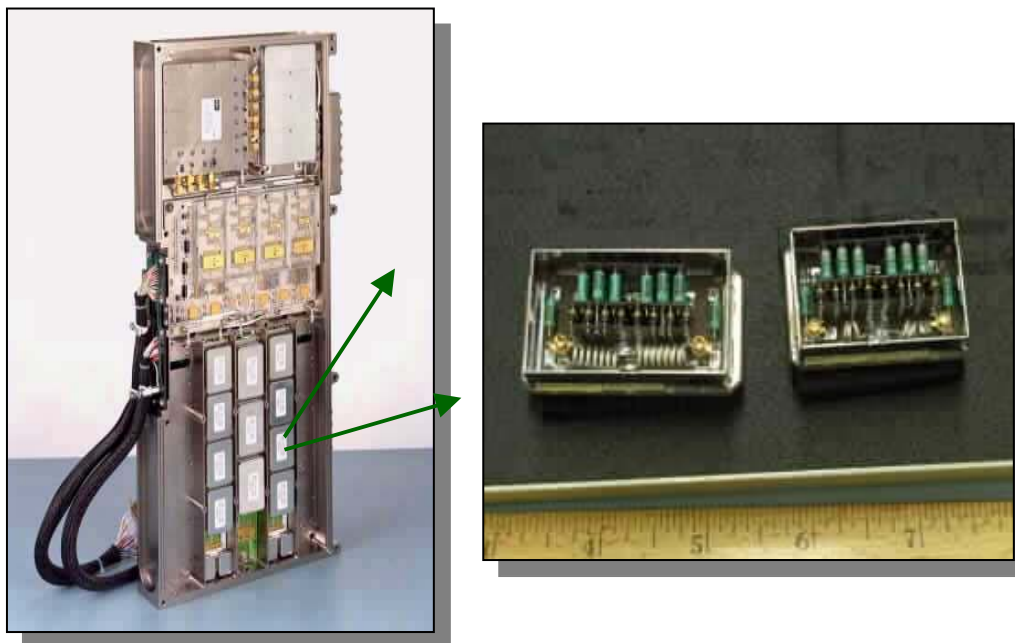
Fig. 6.3: Tracking filter slice of F-22 AIU and detail of varactor-based 2-pole filter assembly

39

In the MEMS insertion demonstration, analog MEMS Tunable capacitors were used replace the function of an array of semiconductor varactor diodes. The goals of this insertion were to achieve increased dynamic range and to dramatically reduce parts count.

6.2   *MEMS-Based Filter Design and Implementation*

A 2-pole, 2.5% bandwidth, UHF tunable bandpass filter prototype was constructed with two of the MEMS variable capacitors to achieve the tuning function.   Each MEMS capacitor in the prototype replaced a 16-varactor diode, series-parallel array and biasing network in the original F-22 assembly.   The wide tuning range and high linearity of the MEMS device enabled a much simpler circuit architecture, Fig. 6.4.
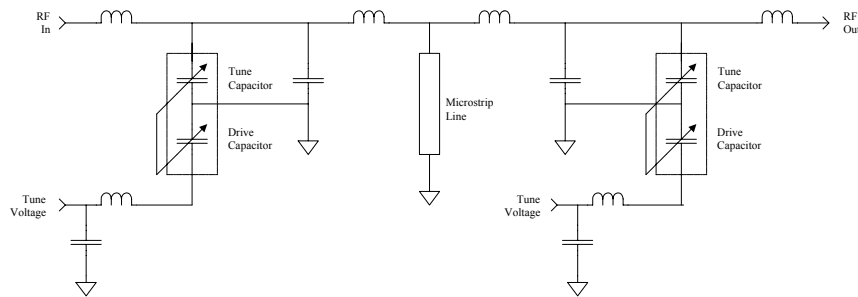
Fig. 6.4: Schematic of MEMS-based 2-pole filter circuit

The circuit, including the component values and package parameters, is shown in Fig. 6.5.
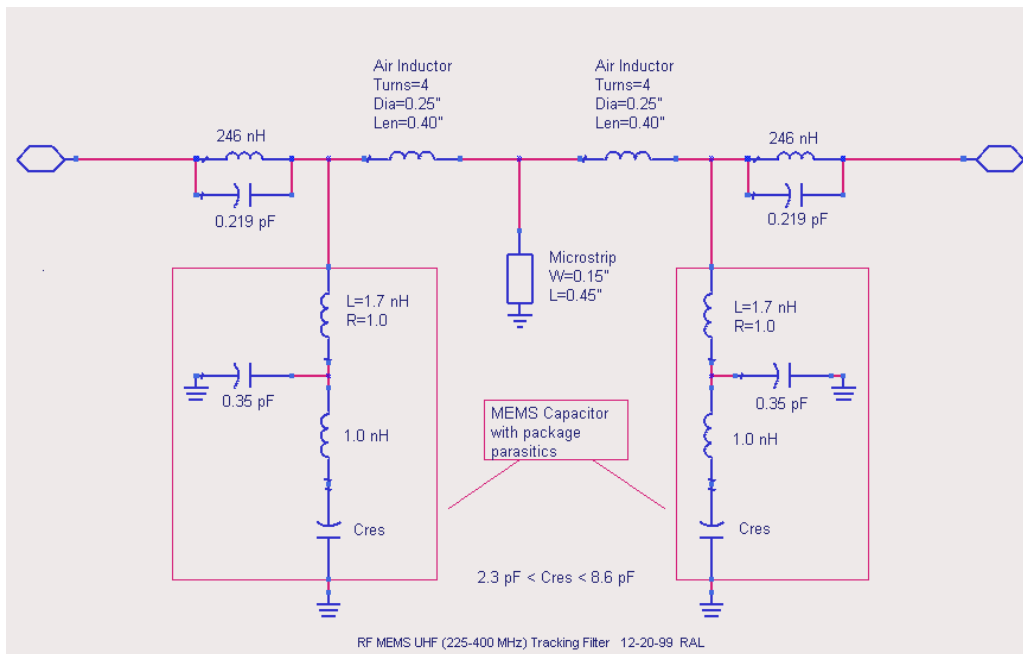
Fig. 6.5: Schematic two-pole filter circuit for the tunable capacitor-based filter

40

The two-pole filter circuit was implemented using the final MEMS tunable capacitors described earlier, Fig. 6.6. For comparison, the equivalent varactor-based filter assembly is also shown in Fig. 6.6, validating the dramatic parts count reduction possible through use of the MEMS technology. This comparison provides a compelling demonstration of the benefits of MEMS in RF applications.
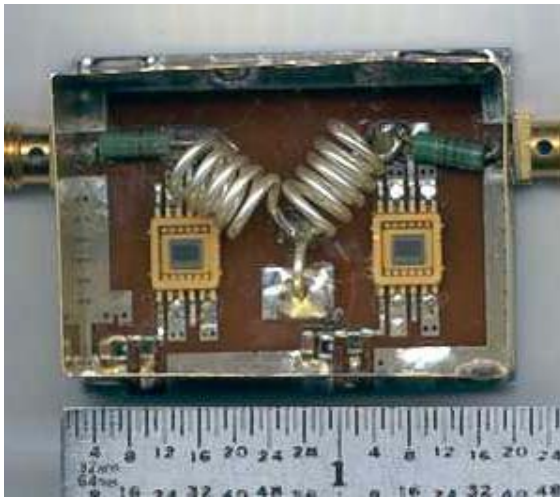
MEMS-Based Filter   *Varactor-Based Filter*
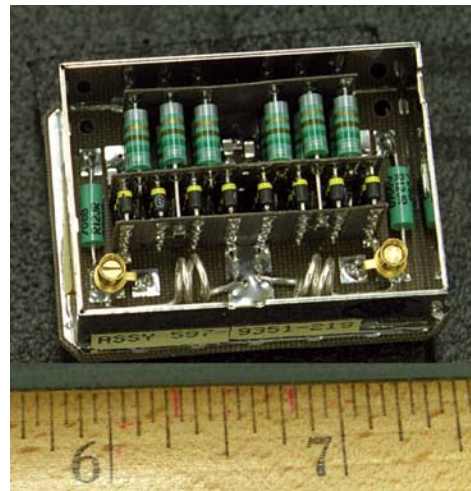
Fig. 6.6: Photograph of MEMS-based two-pole filter assembly and corresponding varactor-based circuit demonstrating substantial parts count reduction

6.3   *MEMS-Based Filter Testing*

Measurements were made of the filter tuning characteristics. These demonstrated the ability to tune across the entire 225-400MHz band with the MEMS based circuit, Fig. 6.7.
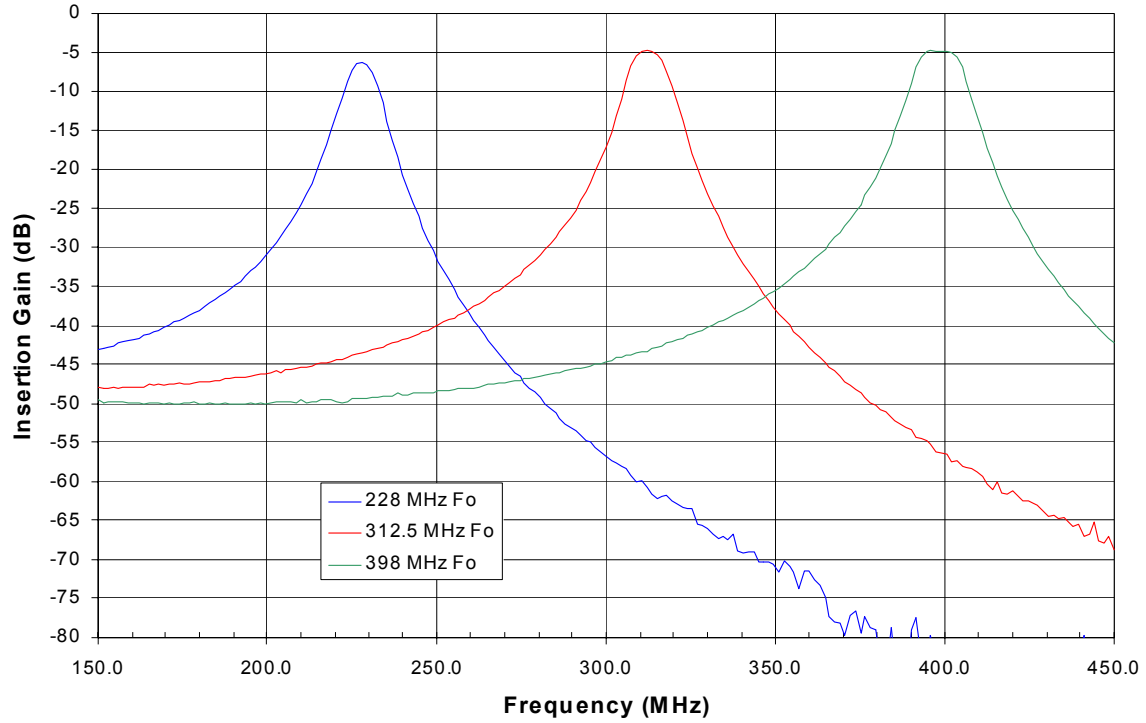
Fig. 6.7: Measured filter loss as a function of frequency across the design tuning range. Limited number of filter positions shown for clarity.

The filter response was measured as a function of tuning voltage to characterize the loss and bandwidth performance, Fig. 6.8. These measurements showed the two MEMS tunable capacitors to be well-matched. The center frequency loss was below the specification for nearly all the tuning range, although it went slightly out of spec. at the low end of the frequency range. Filter bandwidth was below the 3% target for the full tuning range.
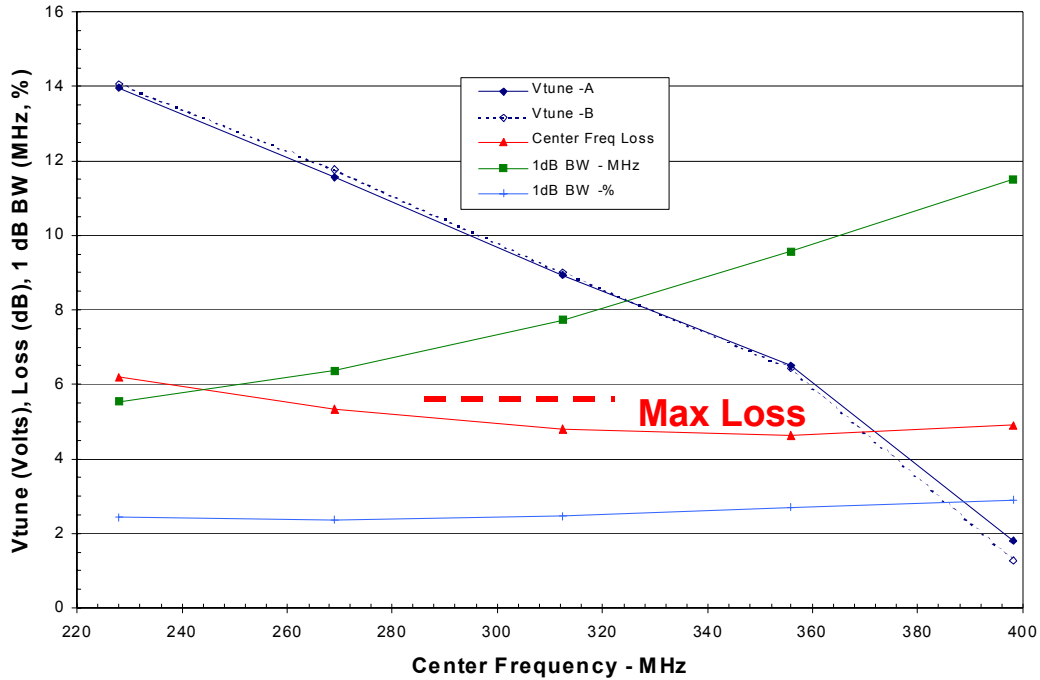
*Fig. 6.8: Measured performance of tunable capacitor-based two-pole filter circuit.
Curve includes tuning voltage vs. center frequency for the two MEMS capacitors,
demonstrating well-matched characteristics; measured and target center frequency loss vs.
center frequency; and absolute and percent bandwidth across the tuning range*

Rejection performance was also characterized, similar to the switch-based filter. This showed a slight exceeding of the +/- 8MHz specification at the highest frequency of the range, but the filter was within spec for all other metrics, Fig 6.9. Linearity measurements confirmed the filter met the +30dBm specification over the full operating range, Fig. 6.9.
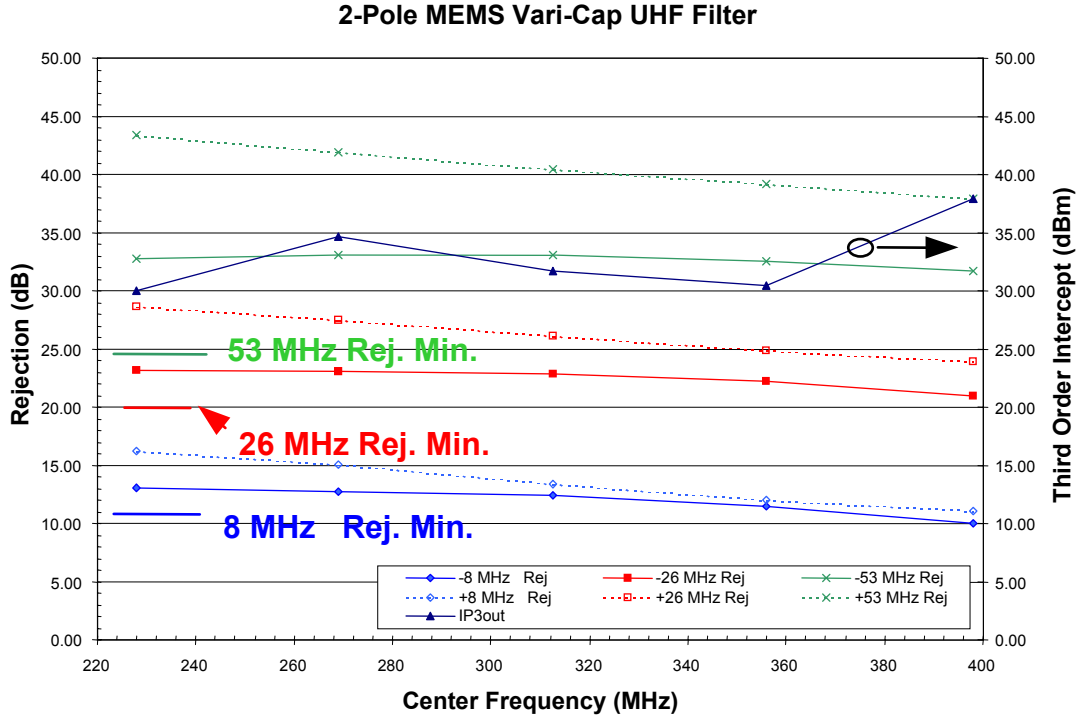
Fig. 6.9: Measured and target rejection of MEMS tunable filter (left axis)
and third order intercept (right axis) across filter tuning range.

Table 6.1 lists performance characteristics for the filter based on F-22 assembly specs. Center frequency and passband measurements (Fig. 6.10) on the 2-pole prototype show the filter has some deficiencies compared to Table 6.1. In general, however, the filter performance compares reasonably well to predicted values given the measured MEMS capacitor characteristics. Tuning range (229-350 MHz) is somewhat less than the desired value due probably to the shunt capacitive parasitic of the large value resonator inductors. Center frequency loss exceeds the 5.5 dB spec below the mid-range center frequencies due to lower-than-desired capacitor Q at the higher capacitance settings. Percentage 1 dB bandwidth does hold nearly constant as expected.

Table 6.1. UHF 2-Pole Bandpass Filter Performance Requirements

Parameter	Value
Center Frequency Tuning Range (min.)	225 to 400 MHz
Center Frequency Insertion Loss (max)	5.5 dB
Passband Ripple Fc ±70 kHz (min)	0.25 dB
Stopband Rejection ±13 MHz (min)	10.75 dB
Stopband Rejection ±26 MHz (min)	20.0 dB
Stopband Rejection ±53 MHz (min)	24.5 dB
Full Range Tuning Time (max.)	27 usec
Output 1 dB Compression Pt. (min)	+ 20 dBm

44

Stopband rejection measurements (Fig. 6.11) show the filter generally meets Table 6.1 requirements. There are 2 points (low and high ends) where the low-side 13 MHz rejection is slightly below the 10.75 dB limit. The low-side 26 MHz rejection at 229 MHz is also slightly below the 20 dB limit. The basic filter topology for constant percentage bandwidth tends to have a slower roll-off below center frequency and thus contributes to the rejection problems. The compensation is a slightly narrower filter bandwidth along with higher Q resonators. Results from third-order distortion measurements (Table 6.2) show good performance above mid-range center frequency. Onset of RF signal-induced capacitance shift at mid- to high capacitance values may contribute to the reduction of IP3 at lower frequencies. It is believed that the improvements in device metallization and flexure stiffness will mitigate both the low Q and power-induced self-tuning that have been observed.

Table 6.2. 3rd Order Intermodulation Distortion and Intercept Point (–3 dBm, Δf=100kHz)

Center Frequency	3rd Order IM Ratio	3rd Order IP (input)
230 MHz	-57.33 dBc	25.7 dBm
290 MHz	-72.00 dBc	33.0 dBm
350 MHz	-84.00 dBc	39.0 dBm
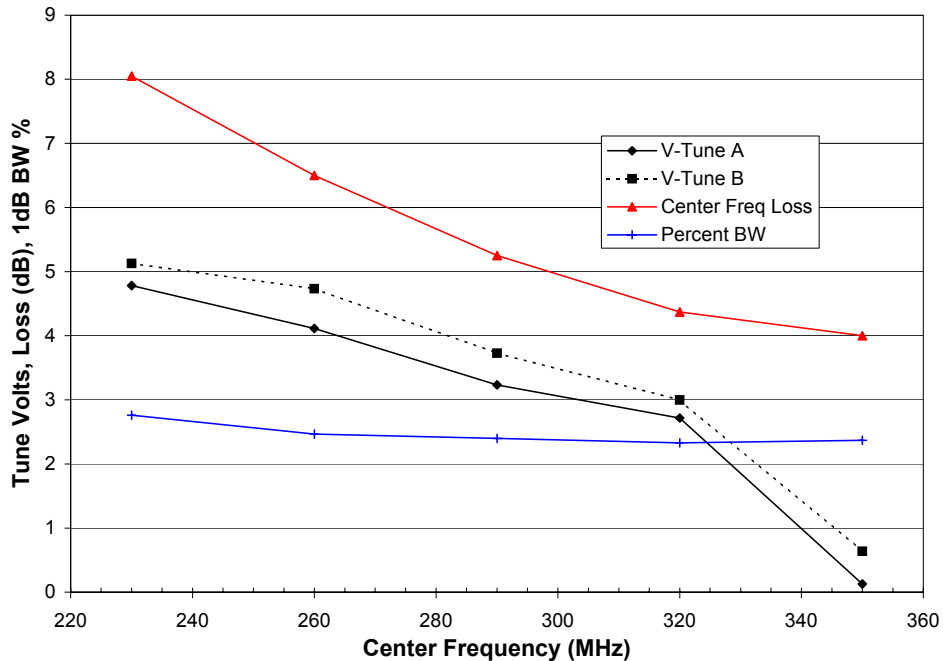
Fig. 6.10: Center Frequency and Passband Performance across the Tuning Range
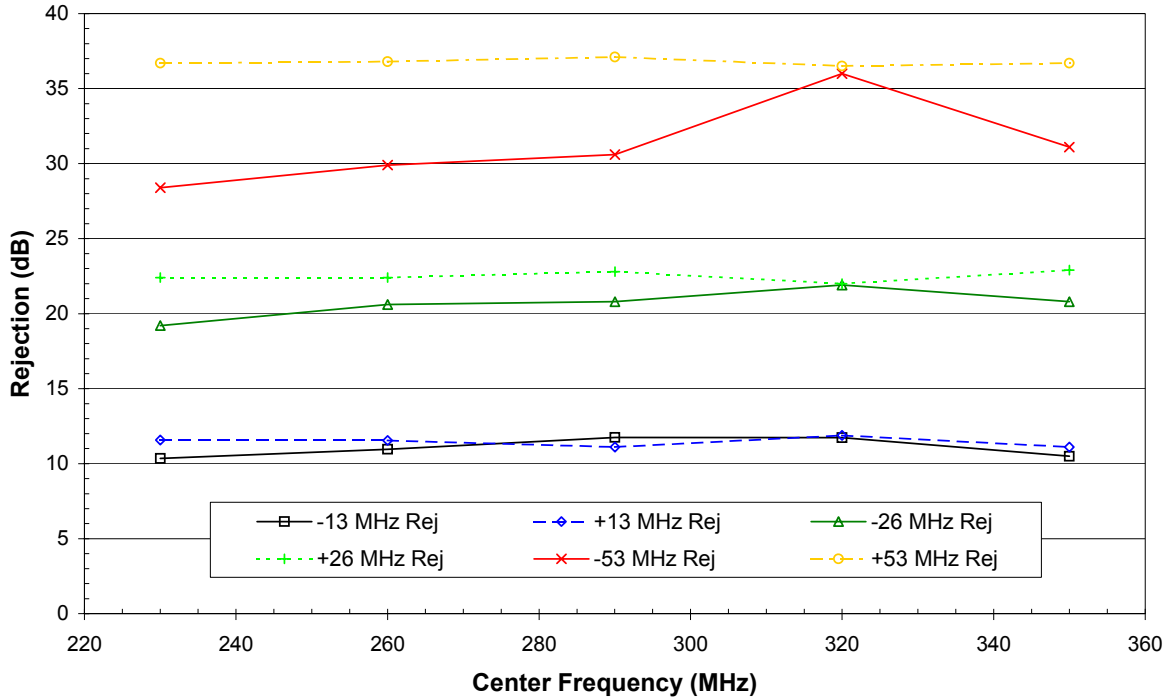
Fig. 6.11: Selectivity performance across the tuning range

A summary of the filter performance is given in Table 6.3.

Table 6.3: Summary of measured performance of MEMS tunable capacitor-based two-pole filter and target specifications from varactor-tuned filter.

	Varactor-tuned design	**MEMS-tuned design**
Rejection:	Meets req'ts	Meets req'ts*
Passband Loss	Meets req'ts	Meets req'ts**
Tune Speed	27 microseconds max.	4.3 milliseconds (ringing)***
Intercept Pt.	+30 dBm	**+30 to +37 dBm**
Parts Count:	62 parts/2-pole (496 parts/8-pole)	**11 parts**/2-pole (**88** parts/8-pole)

* except slightly out-of-spec. at highest center frequency +8 MHz Δf
** except slightly out-of-spec. at lowest center frequency (6.2 dB vs 5.5dB)
***reduced to 600 μs with improved damping

46

The MEMS based filter was slightly out of spec with respect to loss at the lower center frequency position (6.2 vs. 5.5 dB) and with respect to +/- 8MHz rejection at the high frequency end of the tuning range. This could easily be corrected with a slight reduction in series resistance for the tunable capacitor devices in subsequent fabrication runs and re-optimization of the fixed inductor values.

One parameter that was significantly out of spec for the MEMS-based circuit was tuning speed. The present devices showed good speed tuning off of a given frequency, but poor speed tuning onto a new position. This was due in part to excessive mechanical ringing. Improved device designs have been implemented to reduce the ringing and achieve stable tuning within 600 microseconds. Further device optimization will be required to stiffen the mechanical flexures in order to reduce this to under 100 microseconds, and achieving <27 microseconds will be challenging.

7   Picosat Flight Demonstration Support

As an add-on task under this program, RSC supported a MEMS based radio frequency (RF) switch experiment in a miniature satellite format (picosat). This was an initial demonstration of MEMS for space applications. This effort is supported by DARPA-MTO, and the mission is conducted with Aerospace Corporation and Stanford University as partners. MEMS surface micromachined metal contacting switches were fabricated and used in a simple yet informative experiment aboard the miniature satellites to study the device behavior in space and its feasibility for space applications in general. Communication links between multiple miniature satellites as well as between the satellites and ground were also achieved using communications circuits constructed and provided by RSC.

Under this task, RSC supported component delivery on three separate Picosat missions: Picosat-1, MightySat, and Picosat-2. These experiments demonstrated the feasibility of small networked satellites and provided useful information on MEMS switch reliability in space environments.

7.1   *MEMS Switch Considerations for Space Applications*

Device characteristics critical for space use include size, power consumption, and radiation robustness. The RSC microrelay has design characteristics that make it well-suited for space applications. The size of the RSC microrelay is extremely small, with footprint of ~250μm x 250μm. Furthermore, power consumption for RSC microrelay operation is near zero due to its electrostatic actuation scheme. Radiation robustness of MEMS devices is a topic of current research.

7.2   *Picosat-1 Flight Experiments*

As an initial demonstration of the RSC switches in space, the switch devices were used as stand-along test parts, as opposed to mission-critical RF components in the on-board communications circuits. The switch experiments aboard the picosats consist of four MEMS switches in series with four resistors with resistance values of 3 kΩ, 10 kΩ, 30 kΩ, and 300 kΩ to result in four different current levels through each of the switches. The switch-resistor pairs are connected in parallel between a three-volt voltage supply and ground. The mid-point of each of the four switch-resistor pair is tabbed into an on-board analog-to-digital converter (ADC), which outputs in a digital form the switches' equivalent ON and OFF resistances. This information is stored in memory to be transmitted down to the earth through the communication radio transceiver when requested.

The initial Pico-satellite mission, completed on February 10th 2000, demonstrated two pico-satellites tethered together orbiting the earth, periodically collecting data, and downloading this data to another pico-satellite acting as a basestation on the ground. The size of these satellites measures 3 x 4 x 1 inches and little less than half a pound. The

Aerospace Corporation through funding by DARPA engineered the pico-satellites with two major components developed by RSC. The two components are the RF MEMS switches mentioned in the earlier section for the space experiment and the radio communications and networking module that enabled the pico-satellites to communicate and network with a ground basestation. Figure 7.1 shows a picture of the two-board assembly that includes the radio, the MEMS RF switches, and various interfacing electronic components.
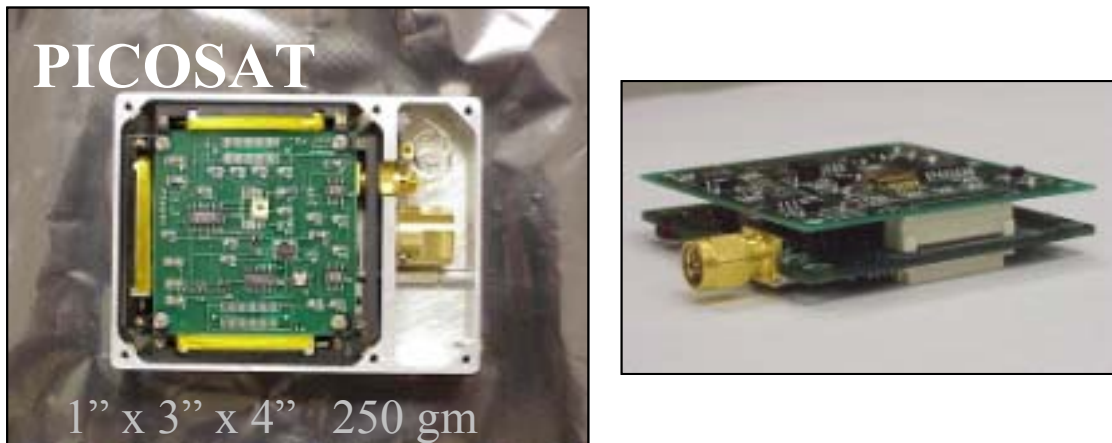
Fig. 7.1: Photo of Picosat module

The pico-satellites were carried on board OPAL, a satellite developed by Stanford University as part of a student-based project. Once launched, the pico-satellites were ejected from OPAL upon command from the ground basestation. Since the pico-satellites have no thruster to perform attitude control, a 100-foot tether has been used to tie the pico-satellites together such that the maximum possible separation between the satellites is kept fixed, given the radios having a limited transmission power of 100 mW. The pico-satellite orbit was a sun synchronous, 750-km polar orbit. With limited transmission power, a 50-meter dish was used for the ground basestation, utilizing facilities at SRI. The 50-meter dish provides approximately 50 dB of antenna gain allowing the orbiting satellites to communicate directly to ground with approximately 1 to 13 dB link margin, the former case for satellites on the horizon and the latter case for satellites directly overhead of the SRI dish.

The orbiting pico-satellites pass within range of SRI basestation twice a day. When locked to the pico-satellites, the duration of contact times between the pico-satellites and the SRI antenna range between 300 to 600 seconds. During each contact time, the pico-satellites download sensor readouts that include the switching statistics of the RF MEMS switch and temperature.

7.2.1   Voltage Step-Up Function for MEMS Switch Control:
Each picosat is powered by a 3-V battery. An inductive charge pump circuit was used to convert the 3-V supply to 100 V for controlling of the MEMS switches. This represents 25% over the threshold drive voltage of 80 V for the switch. The circuit consists of two

stages, Fig. 7.2. The first stage uses a DC biased inductor, L, in series with a switching transistor, Q1, to generate voltage impulses at drain terminal of the switching transistor. The transistor is clocked by using a CMOS multivibrator chip (CD4047BMS). Due to this train of voltage impulses, charge is stored or "pumped" into a capacitor bank, C_{out}. A diode, D1, is used to prevent any reverse current flow. As a result, high DC voltage is seen at the output. The second stage consists of another switching transistor, Q2, which discharges the capacitor when turned on, thereby decreasing the output voltage to zero. Vice versa, the output voltage goes back high when this transistor is turned off. The transistor input is controlled by a command pulse signal, V_{in}. A drain resistor, R_D, is used to limit current flow during transistor turn-on time. This high switching voltage at the output, V_{out}, is then used to drive the MEMS switch. A standard test sequence consists of a switch control signal clocked at 500 Hz. Voltage is measured and stored at the mid-point of the voltage divider comprised of a MEMS switch and the aforementioned series resistor. This voltage provides the health information of the switches under test.
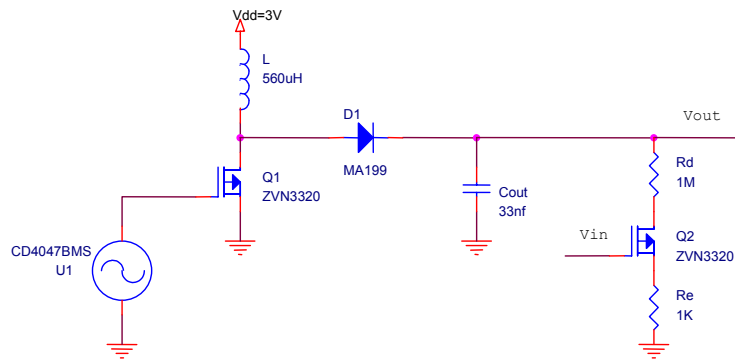
Fig. 7.2: Schematic illustration of the inductive voltage step-up function used for microrelay control.

7.2.2   Network Protocols

A robust low complexity network protocol has been developed to enable the space experiment with commercial low-cost digital cordless chipsets with embedded processor. The protocol is simple yet robust that fits in less than 24 kB and runs with low MIP requirement. In the Picosat-1 mission, the cordless chipset contains an embedded processor based on 65C02 with equivalent 1 MIPS.

The network protocol consists of a basestation that controls a group of pico-satellites (currently two) flying in formation orbiting around the earth. The network provides both direct link to any one pico-satellite or indirect link via multihop through other pico-satellites. When operating with +10dB link margin, the network protocol is capable of supporting up to 50 kbps channel rate from each pico-satellite in direct link to the ground basestation. For the recent mission, scheduling of pico-satellite data transmission has been centralized in the basestation to minimize complexity of the in flight pico-satellites.

7.2.3   State Diagram

The protocol is described in terms of a state diagram shown in Fig. 7.3. The protocol consists of five states: 1) BEACON State, 2) COMMUNICATION State, 3) LISTENING State, 4) IDLE Sate, and 5) SAMPLING State. During each state the pico-satellite performs a series of tasks that can be defined depending on the specific mission requirements. Also, for increased flexibility, the transition between states can be programmed and scheduled at the ground station by uploading a schedule table to the pico-satellites. The scheduling enables mission-specific power management that is particularly critical for the recent mission in which the power source is based completely on battery. For instance, during the non-contact times of the orbit, the pico-satellites can be scheduled to go into the IDLE State, corresponding to a power-down state or sleep mode. Periodically, the pico-satellites can be scheduled to wake up and collect experimental data in the SAMPLING State and go back to IDLE State again. Since the contact times can be estimated once the pico-satellite has been tracked, such schedule can be created to extended several days and updated as necessary. The detail operation of each of the five states is described below.
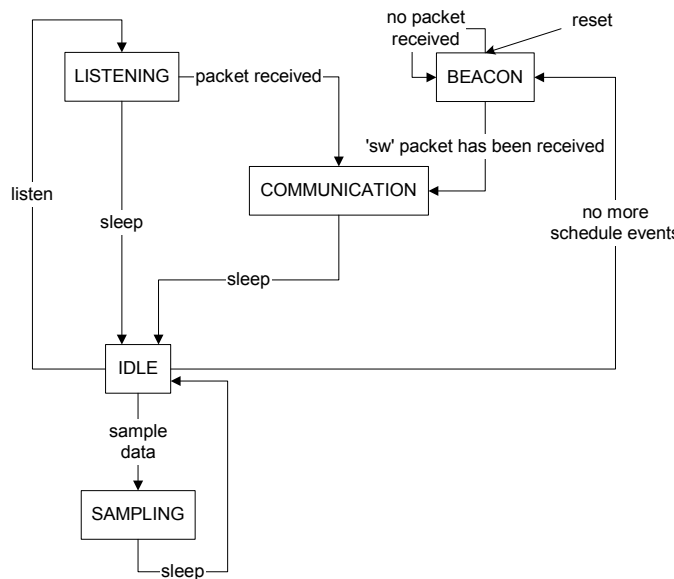
Fig. 7.3   State diagram of the pico-satellite protocol.

BEACON State: Upon power on, the pico-satellites will be in the BEACON State. If a pico-satellite detects a self-reset event, due to a power glitch or any type of internal error, it also goes to the BEACON State. In this state, the pico-satellites transmit beacons that contain both a pilot tone as well as status information, interleaved in time. To conserve power, the pilot tone is transmitted for 80 ms out of 500 ms, where 420 ms is spent in sleep mode. Upon waking up from sleep mode, the pico-satellite then transmit the status information in 20 ms. After transmission, the pico-satellite turns the receiver on for 80 ms to determine if a ground station has detected the prior pico-satellite transmissions. The pilot tone enables radar and antenna tracking systems to locate and actively track the

pico-satellites. If the ground system locates the satellite and determines that it is within transmission range, the basestation will send a SW packet in the uplink. Commands within the packet, if received by the pico-satellite, will be executed accordingly and the pico-satellite will leave the BEACON State. If no packet is received it will remain in the BEACON State. The packet format and type of packets are described in Section 0.

- *COMMUNICATION State:* After receiving a SW packet in the BEACON State or in the LISTENING State, the pico-satellites enter into the COMMUNICATION State. In this state, the pico-satellites transfer data among themselves or with the basestation.

- *IDLE State:* Once the transfer of data is complete, the pico-satellite enters the IDLE State. It also enters the IDLE State if the time allocated for communication in the schedule has been exceeded. In the IDLE State, the pico-satellite is put into deep sleep mode to conserve power. In deep sleep mode, it spends about 0.02 % of the time waking up only to update its internal variables, such as realtime counters and battery levels. The next state depends on the scheduled events and their timing. If the scheduled event corresponds to sampling the sensor module, then the next state is the SAMPLING State. If the schedule event is to get ready for the next contact period, then the next state is the LISTENING State. If there are no other scheduled event, the next state is the BEACON State. Note that the schedule is updated from the ground station when deemed necessary.

- *LISTENING State:* This is the state in which the pico-satellite wakes up from sleep mode (i.e. IDLE State) and prepares for the next contact period by being in the receive mode. If any valid packet is received, then it enters the COMMUNICATION State. If no packet has been received after a specified timeout period then it re-enters the IDLE State. To conserve power, a pico-satellite spends only 16 % of its time in receiving mode while it is in this State.

- *SAMPLING State:* In this state, the pico-satellite samples the sensor data and stores the data on local memory for transfer during the next contact period. After completing the data collection task, it re-enters the IDLE State. To conserve power, a pico-satellite spends only 4% of its time in actually collecting data. The rest of the time, it is in sleep mode.

7.2.4   Packet Format

The protocol transfers data via packets with a general format illustrated in Fig. 7.4. Each packet has a preamble required by the radio to synchronize onto the packet. The header contains a number of fields. The Terminal ID field is 2 bytes and is used to identify the pico-satellite or basestation that either transmitted the packet or will be receiving the packet. The DeviceTask ID is 1 byte and is used to identify the device on the satellite and particular software task that should be processing the data in the payload. The Data Size field ranges from 0 to 244 bytes and contains data that is specific to the packet type. A selected set of packet types is shown in Fig. 7.4. Finally, a 1-byte Flag field is used to

inform the system of the error-control requirement for the packet. Request for acknowledgements can be specified in this field.
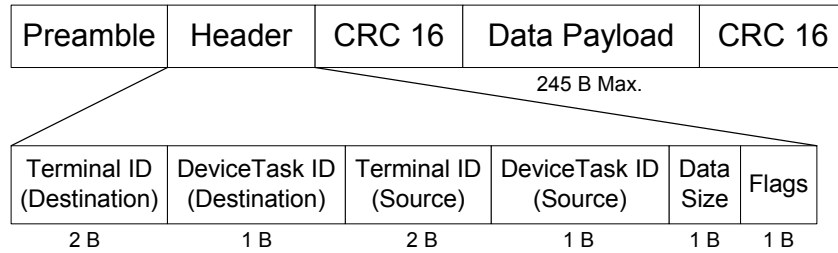
Preamble	Header	CRC 16	Data Payload	CRC 16

245 B Max.

Terminal ID (Destination)	DeviceTask ID (Destination)	Terminal ID (Source)	DeviceTask ID (Source)	Data Size	Flags
2 B	1 B	2 B	1 B	1 B	1 B

Fig. 7.4: General packet format.

7.2.5 Picosat Radio

The network protocols are implemented on an embedded micro-controller as part of a commercially available single-chip spread-spectrum modem for digital cordless telephone. The modem with a companion RF front-end chip and a 1 MB flash RAM has been used to implement a radio module that measures 2.2 x 2.2 x 0.27 inches used to provide all the communications, networking, and task management (e.g. data collection and power management) on board the pico-satellite. The radio module has an RS232 interface which is used to allow other equipment to communicate with the radio for testing purposes or as in the recent mission for tying in a more powerful processor to perform basestation functions. The SRI dish has a radio module connected to a StrongARM processor and a PC acting as the basestation. A schematic of the radio architecture is shown in Fig. 7.5

The radio transmits in the 900 MHz ISM frequency band with a maximum output power of 20 dBm and a transmission bandwidth of 1.3 MHz. The transmission uses direct-sequence spread-spectrum with 11 chips/bit and achieves a raw channel data rate of 100 kbps. The radio has a sensitivity of –105 dBm with 0.001% BER. The path loss at 750 km is 149 dB and with a dish antenna gain of 50 dB and a pico-satellite antenna gain of 7 dB, the link margin is 13 dB. The margin drops to 1 dB when the link is 10-15 degrees above horizon.
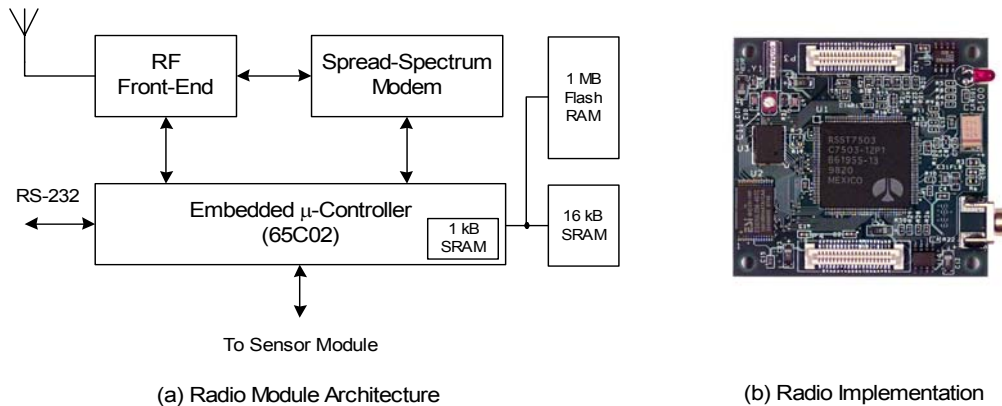

(a) Radio Module Architecture

(b) Radio Implementation

Fig. 7.5: Picosat Radio Module

7.2.6   Mission Summary

On January 26 2000, pico-satellites were launched as part of the payload in OPAL at Vandenberg Air Force Base. Since the exact pico-satellite orbit cannot be determined prior to orbital insertion, the exact pico-satellite orbit is determined after ejection from the mothership via tracking based on 1) passive tracking with NORAD's global radar network and 2) active tracking using the SRI antenna. Passive tracking does not require signaling from the orbiting satellites while active tracking requires RF tones (i.e. beacons) to be transmitted by the orbiting satellites. To facilitate initial communication to the pico-satellites, the mothership orbit is first determined, then pico-satellite ejection is timed to occur over the basestation.

On February 6th, the pico-satellites were released from OPAL.   A number of groundbreaking transmissions were exchanged between the pico-satellites and the ground station.   During these transmissions temperature and RF MEMS switching data were downloaded, validating the networked operation and functionality of the MEMS switch in a space environment.   On February 10th, after the pico-satellites had exhausted its battery power, the mission ended.   Originally, the mission was planed for 21 days. However, it took 24 hours after the release to establish communications with the ground station.   Since prior to contact the pico-satellites are in the BEACON State and were continually transmitting beacons, a major portion of its power has been consumed.

7.3   MightySat Demonstration

A second flight demonstration was subsequently conducted on the MightSat flight. This used similar radios as the Picosat-1 flight. Similar MEMS switches were used, although improved packaging technology was incorporated into the Mightsat parts. These used the preferred epoxy-free die attach and a metal seal lid attach for improved hermeticity and reduced volatiles.

The Mightsat flight differed from the Picosat-1 demonstration in one notable way. For the Mightsat flight, there was a one-year dormancy time in space prior to Picosat ejection. This was to insure that the tethered picosat modules would not interfere with the primary mission of the launch vehicle.

The results of the Mightsat flight demonstrated improved performance over the initial picosat-1 mission. The refined switch packaging resulted in more consistent switch performance. The operation after one-year dormancy validated the suitability of the MEMS switch for space operation.

7.4   Picosat-2 Support

RSC provided hardware for the Picosat-2 flight mission. Here, it was intended to integrate the MEMS switch into critical communications path as a Tx/Rx switch. This

would require the device to operate reliably under significantly higher RF power levels. For the planned mission, operation at ~1W transmitted RF power at 915MHz for a 2 week mission lifetime was required. Assuming beaconing 1/sec, this would translate into survival of at least 1.2 million cycles at high power.

To accommodate the increase power requirement, new switch circuit architecture was developed. This had two switches in parallel in the higher-power Tx path in order to reduce the effective power handling required through each individual switch. For the lower-power Rx path, a single switch was used. A photograph of this device is shown in Fig. 7.6.
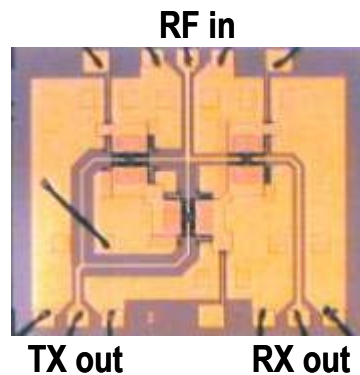

Fig. 7.6: Multi-switch Tx/Rx designed for higher-power operation

Packaged parts were provided to JPL for independent performance testing. Testing of the MEMS Tx/Rx was performed at JPL by Dr. Joanne Wellman under support of their NASA NEPP efforts. These tests demonstrated excellent performance in the switches under high-power conditions. A summary of results include:

- Testing of theTx/Rx switch module at an initial power of 30dBm (1W), cold switching, 915MHz signal frequency was conducted to a total number of cycles of 10 Million. No failures or degradation of the switch was observed
- Power was increased to 32dBm and an additional 7 Million cycles were conducted before any failures were encountered.

8   Summary and Conclusions

This program provided a number of valuable results. First, it significantly advanced the state of MEMS RF switch and Tunable Capacitor device technologies beyond their level at program inception. This has helped broaden the range of applications for these devices in both the military and commercial sectors. Secondly, it has helped benchmark the performance of the RF MEMS devices in actual military communications subsystems, with all operational requirements imposed. This has provided valuable information on the strengths of the RF MEMS devices as well as the critical metrics that will need advancement before insertion into fielded military systems.

For the MEMS RF switch, three device-level parameters were immediately recognized as providing significant system-level benefit. The first, the low insertion loss of the device will improve RF performance by decreasing loss. This is important in the tunable filter application, and will take on increasingly greater significance in higher-frequency devices (where the losses of semiconductor alternatives become larger) and applications requiring large numbers of switches in series (such as multi-bit phase shifter circuits). Second, the electrostatic nature of the switch actuation has beneficial impacts on quiescent power consumption. This will be of considerable benefit in power constrained applications such as hand-held radios and in particular for space-based systems. Third, and of possibly greatest significance, is the extremely high signal linearity of the MEMS switch. For cosite mitigation filters, this becomes of paramount importance. The extremely high linearity of the MEMS switch would translate into substantial system-level benefits. The ability to integrate the switch with on-chip capacitors also offers an attractive path to compact, high-performance filter modules.

The MEMS switch-based filter insertions met all RF requirements of the subsystem. The primary limitations are associated with the present level of cycle-life reliability. The Comanche filter represents probably one of the most challenging applications for the switch due to the rapid hopping requirement, which will result in accumulation of a tremendous number of cycles over the subsystem lifetime (10^{11}-10^{12}). Additional development of the device to extend lifetime will be required to address this region of the application space. The present lifetimes are, however, sufficient to begin considering insertion into less stressing systems. Limited-duration missile seekers and reconfigurable (though not hopping) communications systems are good candidates at present. Other metrics warranting additional development include packaging (especially for low-cost and high-frequency). Power handling is in general limited for the small contact area of the MEMS switch, although the Picosat-2 parts demonstrated that even at present reasonable power levels can be accommodated.

The MEMS Tunable Capacitor device was less mature at program inception, and required considerable device development to accommodate the filter insertion demonstrations. This device was attractive in its wide tuning range. Indeed, for the F-22 UHF filter demonstration, the parts count reduction achieved for the MEMS-based filter clearly illustrated the value of this technology. The non-contact nature of the device also mitigated many of the concerns associated with device reliability.

The RF performance of the tunable capacitor nearly achieved the required filter specifications for the F-22 UHF filter. Insertions losses were slightly out of specification at the tuning extremes due to the device-level series resistance. This can be improved by modification of the device metallization to decrease the resistance. While device signal linearity was within specification, further improvements can be accomplished by improved mechanical design, stiffening the flexures to reduce susceptibility to tuning effective RF voltages.

The primary limitation of the tunable capacitor in the F-22 filter application was associated with the temporal response. The tuning of the device under a step voltage was

quite slow, associated primarily with mechanical ringing and in part to the low mechanical frequency of the structure. Additional design efforts will be needed to increase the device response speed. Initial experiments have been conducted exploring one path to improving this. This addressed using alternate package environments (both gas and liquid) to critically damp the structure. This successfully eliminated device ringing. Modifications to the mechanical design to increase flexure stiffness have also proven beneficial to increasing the response speed.

9 References

1. J.J. Yao et al, Solid State Sensor and Actuator Workshop, June 8-11, 1988, Hilton Head Island, SC, p124

2. L. Dussopt and G.M. Rebeiz, IEEE MTT-S Int. Microwave Symp. Dig., Vol.2, 2002, p120

3. N. Hoivik et al., IEEE MTT-S Int. Microwave Symp. Dig., Vol., 200, p2115

4. J.J. Yao et al, Solid State Sensor and Actuator Workshop, June 8-11, 2000, Hilton Head Island, SC, p246

5. R.L. Borwick et al., Proc. IEEE Int. Conf. On MEMS, Jan 20-24, 2002, Las Vegas, NV, p669